SLAC-PUB-2831
LBL-13464
October 1981
(T/E)

HADRON PRODUCTION BY e^+e^- ANNIHILATION AT CENTER-OF-MASS ENERGIES BETWEEN 2.6 AND 7.8 GeV

PART I: TOTAL CROSS SECTION, MULTIPLICITIES AND INCLUSIVE MOMENTUM DISTRIBUTIONS*

J. L. Siegrist,[k] R. F. Schwitters,[a] M. S. Alam,[b] A. M. Boyarski,
M. Breidenbach, F. Bulos, J. T. Dakin,[c] J. M. Dorfan, G. J. Feldman,
D. Fryberger, G. Hanson, J. A. Jaros, B. Jean-Marie,[d] R. R. Larsen,
V. Lüth, H. L. Lynch,[e,t] D. Lyon,[f] C. C. Morehouse,[g] M. L. Perl,
I. Peruzzi,[h] M. Piccolo,[h] T. P. Pun,[i] P. Rapidis,[j] B. Richter,
R. H. Schindler,[k] W. Tanenbaum[v] and F. Vannucci[ℓ]

Stanford Linear Accelerator Center
Stanford University, Stanford, California 94305

and

W. Chinowsky, G. S. Abrams, D. Briggs,[t] W. C. Carithers, S. Cooper,[e]
R. G. DeVoe,[m] C. E. Friedberg,[n] G. Goldhaber, R. J. Hollebeek,[o]
A. D. Johnson, J. A. Kadyk, A. M. Litke,[p] R. J. Madaras, H. K. Nguyen,[u]
F. M. Pierre,[q] B. Sadoulet,[k] G. H. Trilling
J. S. Whitaker[r] and J. E. Wiss[s]

Lawrence Berkeley Laboratory and Department of Physics,
University of California at Berkeley, Berkeley, California 94720

Submitted to Physical Review D

---

*Work supported by Department of Energy contracts DE-AC03-76SF00515 and W-7405-ENG-48.

Present addresses:

[a] Harvard University, Cambridge, MA 02138.
[b] Vanderbilt University, Nashville, TN 37235.
[c] General Electric, Schenectady, NY 12301.
[d] Laboratoire de l'Accélérateur Linéaire, Centre d'Orsay de l'Université de Paris Sud, 91405 Orsay, France.
[e] DESY, D2000 Hamburg 52, Federal Republic of Germany.
[f] Business Enhancements Compuservice, Escondido, CA 92027.
[g] Hewlett Packard, Palo Alto, CA 94304.
[h] Laboratori Nazionali, I00044 Frascati, Italy.
[i] LBL, Berkeley, CA 94720.
[j] Fermilab, P.O. Box 500, Batavia, IL 60510.
[k] CERN, CH1211 Geneva 23, Switzerland.
[ℓ] L.P.N.H.E., Université Paris VII, F75230 Paris, France.
[m] IBM Research, San Jose, CA 94123.
[n] In House Systems, New York, NY 10038.
[o] SLAC, Stanford, CA 94305.
[p] Stanford University, Stanford, CA 94305.
[q] Centre d'Etudes Nucléaires de Saclay, F91190 Gif-sur-Yvette, France.
[r] M.I.T., Cambridge, MA 02139.
[s] University of Illinois at Urbana-Champaign, Urbana, IL 61801.
[t] University of California, Santa Barbara, CA 93106.
[u] L.P.N.H.E. Université de Paris VI, F75230 Paris, France.
[v] Bell Laboratories, Murray Hill, NJ 07974.

ABSTRACT

Measurements of multihadron production in e^+e^- annihilation at center-of-mass energies between 2.6 GeV and 7.8 GeV are presented. Aside from the narrow resonances $\psi(3095)$ and $\psi(3684)$, the total hadronic cross section is found to be approximately 2.7 times the cross section for the production of muon pairs at c.m. energies below 3.7 GeV and 4.3 times the muon pair cross section at c.m. energies above 5.5 GeV. Complicated structure is found at intermediate energies. Charged particle multiplicities and inclusive momentum distributions are presented.

I. INTRODUCTION

In recent years the study of e^+e^- annihilation into hadrons has substantially enhanced our knowledge of photon-hadron coupling. The pioneering experiments at Frascati,[1] Orsay[2] and Novosibirsk,[3] later followed by work at CEA,[4] helped formulate concrete ideas on hadron production by one-photon annihilation. In conjunction with experiments on deep inelastic electron-hadron scattering, these measurements formed the basis for the quark-parton model.[5] Over a period of several years, the experiment described in this report furnished much detailed information supporting the basic premises of the quark-parton model, in particular the observation of charm, a new quark flavor.

One of the most fundamental ideas of the quark-parton model is the conjecture that hadron production in e^+e^- annihilation proceeds via quark-antiquark pair production where the photon couples directly to the charge of the point-like quarks. A consequence of this picture is that the total cross section for e^+e^- annihilation into hadrons, σ_{had}, must be proportional to the cross section for e^+e^- annihilation into muon pairs, $\sigma_{\mu\mu}$, namely[6]

$$R = \frac{\sigma_{had}}{\sigma_{\mu\mu}} = 3 \sum_q e_q^2 \quad . \tag{1.1}$$

Here the sum runs over all quark flavors involved, and the factor of 3 accounts for three different colors; e_q is the charge of the quarks in units of the electron charge. The ratio R is expected to be constant as long as the c.m. energy, $E_{c.m.}$, does not overlap with resonances or thresholds for the production of new quark flavors. The very first measurements of R, presented in Fig. 1, did indicate that hadron production was substantially larger than expected from a form factor like photon-hadron interaction. However, for various reasons these first experimental results were inconclusive and needed clarification by more detailed measurements. Several new resonances[7-10] were found, $\rho(1600)$, $\psi(3095)$, $\psi(3684)$ and $\psi(3770)$, and the threshold for the production of charmed particles had a pronounced impact between 4 GeV and 5 GeV c.m. energy. It is only below and far above charm particle threshold that the predictions of the quark-parton model can be tested.

The theoretical predictions for the value of R have to be modified to take into account the finite mass of the quarks and the emission of field quanta (gluons) by the produced quarks. In principle, these corrections can be computed in the framework of Quantum Chromodynamics (QCD). A precision measurement of R, well above flavor threshold, constitutes a fundamental test of this theory of strong interactions.

Another aspect of the quark-parton model is the scaling behavior of the single-particle inclusive cross section. The most general form of the differential cross section for the production of a single hadron of scaled energy $x = 2E/E_{c.m.}$ by one-photon annihilation can be written as[11]

$$\frac{d\sigma}{d\Omega dx} = \frac{\alpha^2}{8s}\beta x\left[W_1 + W_0 + (W_1 - W_0)(\cos^2\phi + P_+P_- \sin^2\phi \cos 2\phi)\right] , \qquad (1.2)$$

where α is the fine structure constant, and $s = E^2_{c.m.}$. $\beta = p/E$ is the particle velocity; the particle direction is determined by the polar angle θ relative to the e^+ beam direction and the azimuthal angle ϕ measured in the plane normal to the e^+ direction. P_+, P_- refer to the e^+, e^- transverse polarizations which are directed parallel and antiparallel to the guide magnetic field. W_1 and W_0 are non-negative functions of s, x and the type of particle produced. W_1 measures the coupling to states of helicity one along the direction (θ,ϕ); W_0 measures the coupling to states of helicity zero in this direction. Bjorken[12] has argued that at energies large compared to the particle masses, W_1 and W_0 become functions of only one dimensionless quantity x, and hence cross sections fall like 1/s with energy. The test of this conjecture was another major aim of this experiment.

In this report, measurements of the ratio R over the c.m. energy range from 2.6 GeV to 7.8 GeV, the charged particle multiplicity and the single particle inclusive momentum spectra will be presented.[13] Predictions of the quark-parton model related to the formation of jets will be discussed in a companion paper,[14] referred to as II.

II. APPARATUS

A. The Storage Ring

The Stanford Linear Accelerator Center e^+e^- storage ring SPEAR[15] has been operating at beam energies between 1.3 GeV and 3.9 GeV and peak luminosities between 10^{29} cm^{-2} sec^{-1} and 2×10^{31} cm^{-2} sec^{-1}. In a single vacuum chamber electrons and positrons are confined to one RF bunch each. They counter-rotate in the magnet lattice with a period of 780 ns, and collide at two interaction regions with a luminous volume approximately 0.01 cm high, 0.1 cm wide, and a few cm long. The exact dimensions depend on the operating conditions. The beam energy is monitored by a flip coil measuring $\int B \cdot d\ell$ in a reference dipole magnet connected in series with the ring magnets. The flip coil measurement is corrected for orbit distortions and saturation effects. The uncertainty in absolute calibration of the beam energy is estimated to be ±0.1%. For a given set of runs, the beam energy can be set reproducibly to ±0.1 MeV. The energy spread of the circulating beam is dominated by fluctuations due to the emission of synchrotron radiation. It is given by $\Delta E/E = 2 \times 10^{-4}$ E, where E is the beam energy in GeV.

B. The Detector

The data for this experiment were recorded by the SLAC-LBL magnetic detector (MARK I) at SPEAR during the years 1973 to 1976. Figures 2 and 3 show an end view and a sectioned side view of the apparatus. The solenoidal magnet provided a nearly uniform magnetic field over a volume 3.6 m long and 3.3 m in diameter. Particles emerging from the region of the beam collision passed in sequence through a thin-walled vacuum chamber, cylindrical scintillation counters and two proportional wire chambers surrounding the vacuum chamber, a system of magnetostrictive spark chambers, an array of time-of-flight scintillation counters, the magnet coil, an array of lead-scintillator shower counters, the magnet flux return and finally, a set of planar spark chambers for muon identification. The full momentum analysis, tracking and particle identification capabilities of this detector extended over 65% of 4π solid angle. The azimuthal acceptance was complete; the subtended polar angle ranged from 50° to 130°. Table I presents the radii, lengths, angular range covered and thickness of each of the detector components.

The vacuum chamber was a corrugated cylinder of stainless steel. The four hemicylindrical plastic scintillation counters surrounding the vacuum pipe ("Pipe counters") were each viewed through a Lucite light pipe by a 56 DVP phototube. The primary purpose of these counters was to reduce the trigger rate for cosmic rays. Two sets of proportional wire chambers on the outside of the pipe counters had a wire spacing of 0.21 cm and 0.28 cm, respectively. Their spatial resolution was 700 μm. The main purpose of these chambers was to improve the momentum resolution for tracks not originating from the beam, e.g., from decays of K^o and Λ^o. They were not used in the analysis reported here.

The main tracking elements of the detector were four modules of concentric cylindrical wire spark chambers. Each module consisted of 2 gaps, one with wires at $+2^o$ and -2^o and one with wires at $+4^o$ and -4^o with respect to the beam line. Signals from both ground and high voltage wires were recorded using a magnetostrictive read-out. A gas mixture of 90% neon and 10% helium was used. The chambers had a 1.1 mm wire spacing and an rms spatial resolution in the azimuthal direction of 340 μm. In the z direction, the rms resolution was 1.0 cm and 0.5 cm for the 2^o and 4^o stereo gaps, respectively. The structural support for the chambers consisted of six aluminum posts, 5 cm in diameter with 6 mm wall thickness, at a radius of 79 cm, and a 1.3 cm thick aluminum cylinder enclosing the assembly. The support posts constituted a major source of multiple scattering, and were generally treated as a blind region, subtending 6% of the solid angle.

Just outside the spark chambers was an array of 48 plastic scintillation counters, each 20 cm wide, viewed at each end by a 56 DVP phototube. These counters ("trigger counters") measured flight times for charged particle identification and were used in the detector trigger. Signal pulse heights were recorded in order to enable off-line correction for pulse height dependence. The rms time-of-flight resolution for this system was about 400 psec. Outside the 9 cm thick aluminum coil was an array of 24 shower counters made of five layers, each consisting of 0.64 cm of pilot F scintillator and 0.64 cm of lead. Each counter was viewed on each end by an RCA 4522 phototube. This set of counters measured the energy deposit and was also used in the detector trigger. The energy resolution, averaged over all counters, and measured with Bhabha events, was $\Delta E/E \sim 35\%/\sqrt{E}$.

The muon identification spark chambers, the endcap spark chambers, and the photon detection capabilities of the shower counters were not used in this analysis.

The magnetic field was generated by a solenoid in series with two compensation coils that served to minimize $\int B \cdot d\ell$ along the beam line. Before insertion of the tracking chamber package, field components were measured by a Hall probe at about 5000 points over the tracking volume, 140 cm in radius and from -125 cm to +125 cm along the beam. The variation of the field magnitude was less than 3%. A Legendre polynomial in radius r and longitudinal coordinate z was fit to the field data to yield a parameterization accurate to 0.05% in B_z and 3 Gauss in radial and azimuthal components B_r and B_ϕ. The absolute value of the field was monitored at the center of the magnet by an NMR probe to be 3891 ± 1 Gauss at the operating current of 4350 A. The error in the measured track momenta due to uncertainty in the field was small compared to the position errors in the tracking chambers.

C. Trigger

The trigger rate of the magnetic detector was limited to a few Hz by the time required to recharge the spark chamber pulsing system.

To achieve this low a rate it was necessary to require that at least two charged particles were detected. The trigger was derived from signals from a beam pickup electrode situated upstream of the detector, the pipe counters, the trigger counters, and the shower counters. All coincidences were formed using a 22 nsec wide gate derived from the beam pickup signal. About 200 nsec after beam crossing, various counter latches were interrogated to search for a valid trigger. If none was found, the latches were cleared and the system reset for the next beam crossing. If a valid latch configuration was found, the spark chamber high voltage was pulsed and the time and pulse height digitizers were started. After delay, the counter and spark chamber data were transferred via CAMAC to an XDS Sigma V computer (on the average 3 k bytes per event). A random sample of roughly 20% of the recorded events was analyzed online to monitor chamber and counter efficiencies and the detector performance in general.

A trigger counter latched in coincidence with a shower counter at the same or adjacent azimuthal location was referred to as a Trigger Associated Shower or TASH. Two TASH signals in coincidence with two or more pipe counter latches formed the minimum trigger requirement, resulting in a typical event rate of 1-3 Hz at all energies. The dead time losses were less than 10%.

While the pipe counter coincidence was measured to be more than 99% efficient, the TASH requirement introduced significant trigger biases. For minimum ionizing particles, the TASH coincidence was affected by light losses near the edges of and attenuation along the 3 m long shower counters. This inefficiency was measured using cosmic rays. In addition, hadrons interacted in the magnet coil or for momenta below 200 MeV/c ranged out due to ionization loss before reaching the shower counter. The total TASH efficiency for a single charged particle was measured using events with at least two additional charged particles that fulfilled the TASH trigger. The result[16] is given in Fig. 4 as a function of the particle momentum. The dashed line marks the level of accidental coincidences, measured as the rate at which the TASH coincidence not associated with an incident charged track was latched. Most of these accidental TASH signals in multitrack events were due to photons converting in the detector. By comparison, μ pair events had an accidental probability of roughly 3%.

D. Charged Particle Tracking

The track reconstruction[17] required sparks in at least three of the four wire chamber modules, and only two out of four wires per module. With this high degree of redundancy, these chambers were highly efficient (> 99%) in tracking charged particles, and this efficiency was largely insensitive to variations in the spark efficiency. Furthermore, the track finding was independent of the particle multiplicity as determined by a scan of about 1000 multi-track events. Less than 1% of the reconstructed tracks were judged to be spurious, most of them at small momentum. To avoid this problem, all tracks with less than 150 MeV/c momentum transverse to the beam were ignored. The rms momentum resolution for a 1 GeV/c track was about 15 MeV/c.

In order to separate events produced by beam-beam interactions from beam-gas background, an event vertex was constructed and tracks were classified in the following way. Primary tracks were required to have a radial distance from the beam, R_{min}, of less than 15 cm and a longitudinal coordinate z at R_{min} within $|z| < 60$ cm; all other tracks were classified as secondaries. The interaction vertex was defined as the point which minimized the sum of the perpendicular distances to all primary tracks. For events with two or more tracks, a χ^2 fit was performed to determine the vertex position, taking into account the position resolution and multiple scattering errors.

For annihilation events the momentum measurement was significantly improved by constraining all primary tracks to originate from the beam interaction point. Its position was measured for Bhabha events to an accuracy of 0.5 mm in the transverse coordinates x and y, and to 1 cm in the longitudinal position z. In addition, residual alignment errors of the spark chambers relative to the beam were empirically determined and taken into account in the track fit to improve the angular measurement. The resulting momentum resolution for charged tracks in multiprong events was

$$\frac{\Delta p}{p} = \sqrt{(0.013\ p)^2 + (0.006)^2} \quad ,$$

where p (measured in GeV/c) referred to the component of momentum transverse to the main component of the magnetic field. The first term is the contribution from the position error, the second term gives the multiple scattering error. For particles with a large momentum component parallel to the magnetic field, the resolution degrades with decreasing angle relative to the beam.

III. EVENT SELECTION

Using the measured charged particle momenta, the associated time-of-flight, the shower counter pulse height and the reconstructed vertex position, two general categories of events were selected, namely e^+e^- annihilation to three or more hadronic particles,

$$e^+e^- \rightarrow \gamma^* \rightarrow \text{hadrons} \tag{3.1}$$

and lepton pair production,

$$e^+e^- \rightarrow e^+e^- \tag{3.2}$$

$$e^+e^- \rightarrow \mu^+\mu^- \tag{3.3}$$

$$e^+e^- \rightarrow \tau^+\tau^- \quad . \tag{3.4}$$

While the reactions (3.2) and (3.3) were easily identified and separated from the hadronic event sample, most of the τ-pair events remained in the hadronic sample and had to be treated by a background subtraction.

Of the total data recorded, roughly 5% were hadronic events (3.1), 10% were Bhabha scattered electrons (3.2), μ-pairs (3.3) or τ-pairs (3.4), and the remaining events were cosmic rays and beam associated background, most of which was removed in the first stage of the analysis. Events with two collinear prongs (within 10^o) and a difference in the measured time-of-flight of more than 8 nsec, as expected from a single particle crossing the detector, were rejected as cosmic rays. Most of the beam associated backgrounds were removed by requiring that the event vertex be located at a radial distance of less than 15 cm and at a longitudinal distance of less than 40 cm from the detector center. In addition, the trigger condition was strengthened by the requirement that there be two TASH coincidences with a charged particle track projecting to each.

Events with three or more prongs forming a vertex were classified as multi-hadron events. Two-prong events with total charge zero and track momenta greater than 300 MeV/c were also included in the hadronic event sample if the difference in azimuthal angle was greater than 20° and less than 160°. Specific cuts were designed to remove various electromagnetic backgrounds, such as lepton pair production in the two-prong sample, and Bhabha events with a radiative photon that converted in the beam pipe or the pipe counter, in the multiprong sample. The momentum cut on the two-prongs reduced the dominant background due to interactions of the beam with the residual gas or the vacuum pipe, and the contamination from the two-photon exchange process. Furthermore, this cut lowered the sensitivity of the two-prong sample to variations in the TASH trigger efficiency.

In order to evaluate the purity of the hadronic event sample and to estimate the possible losses of events introduced by the above selection criteria, a sample of triggers containing some 1000 hadronic events was hand-scanned by physicists. Ten background events had been incorrectly classified as hadronic events, while ten hadronic events had been rejected as background. On the basis of this test, a systematic error of 2% was assigned to the hadronic event selection.

The hadronic event sample selected by the above cuts still contained background from collisions of the beam with the residual gas or the vacuum chamber, from two-photon exchange processes, and $\tau^+\tau^-$ production and decay. In the following we shall discuss how these background sources were reduced and/or corrected for.

The beam associated background had two components that can be inferred from Fig. 5, which shows the position of the reconstructed event vertex as a function of a) the radial distance R from the beam, and b) the longitudinal distance z from the interaction point. While the sharp peak at small R is due to beam-beam interactions, the enhancement near R of 8 cm is due to interactions of off-momentum beam particles in the vacuum chamber and the pipe counter. This background was eliminated by requiring that R be less than 4 cm. From the hand-scan of events and the observed vertex distribution, we estimated the loss of hadronic events caused by this cut to be 5 ± 3%. Interactions of beam particles with the nuclei of the residual gas yielded vertices uniformly distributed along the z-axis. This was verified by a study of events recorded during single beam operation of SPEAR. As a result, beam-beam events were selected to have vertices with a longitudinal coordinate z in the interval $-0.12\text{m} \leq z \leq +0.10$ m. Their contamination by beam-gas events was extrapolated to be less than 5% from the observed yields in the regions $-0.17\text{m} < z < -0.12$ m and $0.10\text{m} < z < 0.17$ m. This background was subtracted bin-by-bin in the observed multiplicity and momentum distributions of all charged particles.

The background from two-photon exchange processes was estimated by Monte Carlo calculation. The contribution from the four-lepton final states $e^+e^-e^+e^-$ and $e^+e^-\mu^+\mu^-$ amounted to less than 2% of all hadronic events, and was subtracted from the observed two-prong sample, since the scattered beam particles were not detected. The observed contribution from hadron production by two-photon interactions was expected to be small by comparison ($\lesssim$ 1%) and was neglected.

The number of events originating from the production and decay of the τ lepton[18] was determined by a Monte Carlo simulation, which included the dominant decay modes $e\nu\bar{\nu}$, $\mu\nu\bar{\nu}$, $\pi\nu$ and $\rho\nu$, plus a multipion decay with a branching ratio of 23%. The contribution of τ lepton events was estimated to account for 10% of all detected hadronic events, predominantly at low multiplicities. At 7.4 GeV, for example, the τ contamination amounted to 34% of the two-prong events, 10% of the three- and four-prong events, and 2% of the events with higher multiplicities. Since the efficiency estimates made use of the observed charged multiplicity, we chose to subtract the τ-lepton background from the sample of detected events rather than from the efficiency corrected cross section.

IV. DETECTION EFFICIENCY

In order to relate the observed yield of hadronic events or any observed particle distribution to the cross section for hadron production by one-photon annihilation at a fixed c.m. energy, the detection efficiency and the effects of initial state radiation had to be determined. We defined the detection efficiency as the probability that a hadronic final state was observed in the detector and passed all selection criteria. Due to the limited solid angle of the detector and the TASH trigger requiring two charged particles, the efficiency depended on the particle multiplicity, and the angular and momentum distributions. As a result, the uncertainty in the knowledge of this efficiency and its dependence on the c.m. energy was the main contributor to the systematic error in the determination of the total hadronic cross section.

A. Monte Carlo Simulation

Monte Carlo techniques were used to estimate the detection efficiency for hadronic events. This task was twofold: it required the generation of events according to models for hadron production and the simulation of the response of the detector to these events. The simulation of the hadronic final state was not a straightforward procedure, but rather an iterative process, since the dynamics underlying the production of hadrons were unknown. Several models for the hadronic final states involving different particles, various multiplicity distributions, and various angular and momentum correlations were tried. The resulting particle distributions were compared with experimental data to choose the most appropriate model and to adjust the free parameters for each c.m. energy.

For simplicity, we started out with a model that assumed that all final state particles were pions and that their momenta were determined by phase space kinematics. For each event to be generated, the total multiplicity n was selected from a Poisson distribution, and the ratio of charged to neutral pions was chosen according to a binomial distribution. Charge conservation was enforced. States containing neutral pions only were discarded, since they are not allowed by charge conjugation invariance. The particle momenta and angles were generated according to invariant phase space.[19]

In order to simulate jet-like dynamics observed at c.m. energies above 5 GeV, the phase space model was modified by insertion of a matrix element[20] squared of the form

$$|M|^2 \propto \exp\left\{-\sum_i \frac{p_{\perp i}^2}{2b}\right\} \quad , \qquad (4.1)$$

where $p_{\perp i}$ is the momentum component transverse to the jet axis for the ith particle, and the sum runs over all produced particles. The parameter b was set to reproduce the average transverse momentum of 350 MeV/c observed in the data, independent of c.m. energy. The angular distribution of the jet axis was chosen in accordance with the most general form allowed for one-photon exchange, namely

$$f(\theta) \propto 1 + \alpha \cos^2\theta \quad ; \qquad (4.2)$$

here θ is the polar angle relative to the incident beams. The Monte Carlo simulation used $\alpha = +1$, in agreement with our measurement.[14] Details of the jet analysis will be presented in II.

The remaining two free parameters describing the hadronic final states, the mean total multiplicity and the ratio of charged to neutral pions, were adjusted so that the simulation and data agreed on the observed mean multiplicity and the mean momentum for charged particles at each c.m. energy. Below 5 GeV, the angular and momentum distribution predicted by the phase space and the jet model were very similar and agreed with data; above 5 GeV, the observed distributions for total and transverse momenta clearly favored the jet model simulation[14] and hence, this model for the production mechanism was used at all energies.

The simple all-pion jet model was modified to include the production of heavier particles, such as η^0, kaons and nucleons.

The different particle multiplicities were chosen according to binomial distributions, subject to the constraints of charge, strangeness and baryon number conservation. By proper adjustment of the average multiplicities for each particle type, good agreement with the data on charged particles could be obtained. Based on the relatively small difference between the predictions of the two models, and the reduced computational effort, the simpler all-pion jet model was used.

Aside from the event generator the Monte Carlo calculation included a complete simulation of the detector properties, such as geometrical acceptance, hardware inefficiencies, trigger conditions and event selection criteria. All produced particles were traced through the scintillation counters and tracking chambers. Particles traversing a pipe, trigger or shower counter set latches with probabilities given by the measured pipe counter and TASH efficiencies. All hits were tallied to determine whether the event fulfilled the trigger conditions. The decay of neutral pions, Dalitz pairs, and photon conversions in the beam pipe and the surrounding material were taken into account. Charged particles that passed through at least three of the four spark chamber modules were retained, provided their momentum component transverse to the beam exceeded 150 MeV/c. Gaussian resolution functions of appropriate width were applied to the produced particle momenta and angles. In order to simulate the observed vertex distribution, the events were distributed along the beam axis with a Gaussian distribution function. Events satisfying the trigger requirements were analyzed and submitted to selection criteria identical to the actual data analysis.

In order to check the correctness of the Monte Carlo program, simulated events were compared to selected data. The geometrical acceptance was well reproduced: the distributions in momentum, and in azimuthal and polar angle agreed well within the statistical errors. The observed multiplicity of charged particles was in reasonably good agreement, however, the Monte Carlo overestimated slightly the even multiplicities and underestimated the odd ones. This effect was common to all production models, and was an indication that some details of the detector or the final state were not perfectly simulated.

B. The Unfold Method

Since the detection efficiency for hadronic events was sensitive to the charged particle multiplicity, a special procedure was developed that made maximum use of the experimental data and did not rely on the Monte Carlo simulation to exactly reproduce the charged particle multiplicity. We defined ε_{qp} as the probability that a hadron final state, produced at a total energy $E_{c.m.}$ with the charged particle multiplicity p, be detected (and passed all selection criteria) with q charged tracks. Thus M_q, the number of events observed with charged multiplicity q was related to N_p, the number of events produced with charged multiplicity p, in the absence of initial state radiation, by

$$M_q = \sum_{p=2}^{\infty} \varepsilon_{qp} N_p \quad . \tag{4.3}$$

The determination of N_p from the observed quantities M_q proceeded in two steps. First, the efficiencies ε_{qp} were determined by

Monte Carlo simulation of the production and detection of the final state hadrons. Secondly, a maximum likelihood method was applied to invert or unfold the simultaneous equations (4.3), subject to the constraint $N_p \geq 0$. The likelihood function was defined as the product of Poisson functions for the detected events,

$$\mathscr{L} = \prod_q \frac{\mu_q^{N_q}}{N_q!} e^{-\mu_q} , \tag{4.4}$$

where μ_q was the predicted number of detected events with multiplicity q. As a result of this "unfold", we obtained the average detection efficiency at a given c.m. energy,

$$\bar{\varepsilon} = \frac{\sum M_q}{\sum N_p} . \tag{4.5}$$

Before we present the results, we shall have to discuss in some detail the method used to take into account radiative processes in the initial state.

C. Radiative Corrections

Emission of photons, both virtual and real, leads to modification of the lowest order cross sections and inclusive distributions. Radiative corrections are usually categorized into single hard-photon emission, multiple soft-photon emission, vertex corrections and vacuum polarization. The net radiative correction to one-photon exchange, calculated by Bonneau and Martin,[21] is,

$$\sigma_M(s) = \sigma_0(s)(1+\delta) + t \int_{\Delta}^{E} \left(1 - \frac{k}{E} + \frac{k^2}{2E^2}\right) \sigma_0(s - 4Ek) \frac{dk}{k} . \tag{4.6}$$

This expression relates, in third order, the experimentally measured cross section $\sigma_M(s)$ to the one-photon exchange cross section $\sigma_0(s)$, where E is the nominal beam energy and $s = E^2_{c.m.} = 4E^2$. The first term with

$$\delta = \frac{2\alpha}{\pi}\left(\frac{\pi^2}{6} - \frac{17}{36}\right) + t\left(\frac{13}{12} + \ell n\,\frac{\Delta}{E}\right) \qquad (4.7)$$

includes vertex modifications, vacuum polarization, and soft photon emission. These contributions effectively modify the flux of single virtual photons involved in one-photon exchange. The effective radiator thickness t is given by

$$t = \frac{2\alpha}{\pi}\left(\ell n\left(\frac{s}{m_e^2}\right) - 1\right) , \qquad (4.8)$$

where m_e is the mass of the electron. The second term in Eq. (4.6) accounts for the emission of real photons with energy k greater than the cut-off Δ. Due to hard photon emission, the e^+e^- annihilation occurs at an energy less than $E_{c.m.}$, where the cross section may be different.

While radiative effects in the final state were ignored, radiative corrections for the initial state were included in the efficiency calculation. The emission of real photons parallel to the incident beam was included in the Monte Carlo simulation, and hadronic events were generated according to the all-pion jet model with parameters adjusted for the radiative energy loss. The number of events produced without a radiative photon above a cut-off energy Δ is proportional to $\sigma_0(1 + \delta)$, where δ depends only on the cut-off Δ and the beam energy E. Thus we can rewrite the efficiency ε_{qp} as

$$\varepsilon_{qp} = \frac{M_{qp}}{N_p}\,\frac{N_p}{N_p^o}\,(1 + \delta) = \tilde{\varepsilon}_{qp}\,\Omega_p \quad , \qquad (4.9)$$

where M_{qp} is the number of detected events with q charged prongs that were produced with a charged multiplicity p. N_p^o refers to the number of events of multiplicity p produced without hard-photon emission, while N_p refers to all produced events of multiplicity p. Instead of evaluating equation (4.9) directly using Monte Carlo simulated data at different c.m. energies, we chose to factorize the efficiencies ε_{qp} into two terms, $\tilde{\varepsilon}_{qp} = M_{qp}/N_p$ and $\Omega_p = N_p(1+\delta)/N_p^o$.

The efficiencies $\tilde{\varepsilon}_{qp}$ included the effects of the detector geometry, the counter efficiencies, trigger criteria and event selection. The $\tilde{\varepsilon}_{qp}$ depended only weakly on the shape of the hadronic cross sections σ_0 and were determined by Monte Carlo simulation at various c.m. energies. As an example, Figure 6 shows the efficiencies $\tilde{\varepsilon}_{0p}$ versus $E_{c.m.}$. $\tilde{\varepsilon}_{0p}$ are the probabilities that an event produced with p charged particles is not detected. The curves represent a smooth interpolation of these Monte Carlo results and they were obtained by a spline fit.[22]

The functions Ω_p were independent of the detector properties, but they reflected shape of the hadron cross section for each multiplicity at energies below $E_{c.m.}$. Since the multiplicity dependence of σ_0 was much less certain than the total cross section, we chose to factor each Ω_p into a term ω, that reflected the variation of the cross section σ_0 and was independent of the charged particle multiplicity, and a term $\tilde{\Omega}_p$ that varied slowly with energy,

$$\Omega_p = \omega\,\tilde{\Omega}_p \quad . \qquad (4.10)$$

This factorization was possible to the extent that changes in the produced multiplicity with c.m. energy were small compared to the variation in cross section. Due to this factorization the radiatively corrected efficiencies ε_{qp} were obtained without the need to repeat the Monte Carlo calculations for each new estimate of σ_0.

In practice, the determination of ω $(E_{c.m.})$ from the integral in Eq. (4.6) required an estimate of the hadronic cross section σ_0 as a function of the c.m. energy. Its exact shape is *a priori* not known, in particular between 3.5 GeV and 4.5 GeV, where earlier measurements[23,24] had indicated structure. In order to obtain this estimate of σ_0, we determined the yield of hadronic events relative to the QED cross section for muon pair production by using a smooth detection efficiency without radiative corrections. The result, presented in Fig. 7 for the c.m. energy range from 3.4 GeV to 4.6 GeV, indicated enhancements near 3.77, 4.1 and 4.4 GeV. Combining this measurement with previous measurements in the MARK I detector[23,24] we derived a smooth representation of the cross section σ_0. This is shown in Fig. 8. In trying to avoid the creation of peaks from mere statistical or systematic fluctuations, we chose to include as little structure as possible into the estimate for σ_0. As a result, we may have underestimated the structure that was present.

The multiplicity dependence of the radiative correction Ω_p is presented in Fig. 9a, where Ω_2 reflects the resonance structure of σ_0 near 4 GeV. This rapid variation of the correction was factored out according to Eq. (4.10) such that the functions $\tilde{\Omega}_q$ varied smoothly with energy, and the variation of the total cross section was retained in the factor $\omega(E_{c.m.})$, given in Fig. 9b. Not included in the correction function $\omega(E_{c.m.})$ were the radiative tails of the $\psi(3095)$ and $\psi(3684)$ resonances; they would have caused very large variations of ω at energies close to the mass of these states. For reasons of computational economy, this correction was evaluated separately, and subtracted from the efficiency corrected cross section. The cross section of the $\psi(3095)$ and $\psi(3684)$ at energies far above their masses was calculated analytically,[25]

$$\sigma_R(E_{c.m.}) = \sum_{\psi,\psi'} \frac{6\pi^2\Gamma_{ee}}{M^2} \frac{t}{k} \left(\frac{k}{E}\right)^t \left[1 - \frac{k}{E} + \frac{k^2}{2E^2}\right] \phi(E_{c.m.}) \qquad (4.11)$$

Here $E = E_{c.m.}/2$, $k = E - (M^2/4E)$ is the photon energy, and M and Γ_{ee} are the mass and leptonic width of the resonances.[26] The factor ϕ accounts for the change in detection efficiency due to the c.m. motion of the produced resonance state. ϕ was determined by Monte Carlo calculation and ranged from 0.5 at energies above 7 GeV to 1.0 close to the resonance mass.

D. Resulting Efficiencies

The detection efficiency for hadronic events averaged over the multiplicities, as given by Eq. (4.5), is presented in Fig. 10 as a function of the c.m. energy. The data presented are results from the maximum likelihood fit of the observed charged multiplicity to the Monte Carlo simulated data. The effect of the resonance structure near 4 GeV, as described by the factor $\omega(E_{c.m.})$, and the radiative tails of the $\psi(3095)$ and $\psi(3684)$ have not been included here for reasons of clarity. As the c.m. energy increases, the average detection efficiency $\bar{\varepsilon}$ rises gradually until it reaches a plateau of 73% above 6 GeV. This rise is caused by an increase in mean charged momentum and multiplicity that raises the efficiency of the TASH trigger. The smooth curve represents an interpolation to the measured points; the errors indicated are statistical only.

Estimates of the systematic uncertainty in the hadron detection efficiency were obtained by studying its sensitivity to the choice of the

Monte Carlo production model and the adjustable parameters. The individual elements of the efficiency matrix ε_{qp} showed variations up to 12% depending on the particular model. The average detection efficiency obtained by the unfold technique varied as much as ±8%. This sensitivity was half as large as in cases where $\bar{\varepsilon}$ was determined directly from the Monte Carlo simulation as the detected fraction of all generated events.

The determination of the efficiency for detecting a single charged particle of momentum $x = 2p/E_{c.m.}$ was based on measured distributions only to the extent that the observed mean charged particle multiplicity, the total momentum and the transverse momentum relative to the jet axis have been used to adjust the free parameters in the jet model at various c.m. energies. The inclusive charged particle efficiency $\varepsilon(x)$, including corrections for initial state radiation, was defined as

$$\varepsilon(x) = \frac{M(x)}{N_0(x)}(1+\delta) \quad , \qquad (4.12)$$

where $M(x)$ is the number of charged particles of momentum x, detected in events with at least three charged particle tracks. $N_0(x)$ refers to the number of charged particles produced in events without a radiative hard photon, and δ is defined in Eq. (4.7). Figure 11 shows $\varepsilon(x)$ for three different c.m. energies. The rather rapid drop of $\varepsilon(x)$ with increasing x was primarily caused by the requirement that at least three charged particles be detected. Radiative corrections, electrons from converted photons and Dalitz decays, and the jet angular distribution further enhanced $\varepsilon(x)$ for low x. The TASH efficiency and the finite momentum resolution tended to favor the high x region over the low x region. The overall variation of $\varepsilon(x)$ with c.m. energy was caused by the TASH trigger requirement. The uncertainty in the detector response and the hadron production model contributed roughly equally to the systematic error on $\varepsilon(x)$. The error on $\varepsilon(x)$ was estimated to be of the order 10-15%, it was largest for small and large values of x.

V. NORMALIZATION

The time integrated luminosity was based on large angle Bhabha scattering and μ-pair production. These processes were separated from multi-hadronic background by their distinctive topology: two oppositely charged particles, with momenta greater than 1/2 the incident beam energy and collinear to within 10°. Shower counter information was used to distinguish muons from electrons; time-of-flight measurements were used to reject cosmic rays. The TASH efficiency for electrons was measured to exceed 99.5%; for $\mu^{\pm}$, it varied as a function of polar angle between 94% and 98%. No beam related background was observed.

Based on QED cross sections with radiative terms according to Berends, Gaemers and Gastmans,[27] the total number of Bhabha events within the interval $|\cos\theta| < 0.6$ was used as a normalization. Comparisons between the QED prediction and the observed shape of the polar angle distribution for e^+e^- and $\mu^+\mu^-$ and the ratio of e^+e^- to $\mu^+\mu^-$ events showed very good agreement with QED at all c.m. energies.[28] The luminosity deduced from the Bhabha events detected in the central detector was checked by comparing to Bhabha events detected by two pairs of scintillation shower counters positioned at 20 mrad above and below the beam axis. This real-time luminosity monitor had a counting rate of 10 Hz or more and provided high statistical accuracy. As a result of the fourfold symmetry of this monitor, the summed counting rate in both telescope arms was, to first order, independent of the exact beam position and direction.

The absolute normalization of the monitor was, however, uncertain to 10-15%, due to its limited size and the sensitivity of the counting rate to its position errors. The principle function of the luminosity monitor was to provide a relative normalization on-line.

Bhabha scattered events in the central detector were chosen as the best measure of the integrated luminosity because their measurement had the smallest statistical and systematic errors. The systematic error in this measurement, roughly 6%, was dominated by the uncertainty in the radiative corrections and long-time variations in the detector efficiency.

VI. RESULTS

From the number of observed multihadron events, N_{HAD}, that had been corrected for backgrounds caused by beam-gas collisions and lepton pair production by one-photon and two-photon interactions, and for losses due to the cut on the position of the interaction vertex, we obtained the hadronic cross section using the relation,

$$\sigma_{HAD} = \frac{N_{HAD}}{\bar{\varepsilon}\,\omega\,L} - \Delta\sigma_{\psi} \quad . \tag{6.1}$$

The product $\bar{\varepsilon}\omega$ refers to the average detection efficiency corrected for radiation effects, and L is the integrated luminosity determined from large angle Bhabha scattering. The radiative contributions $\Delta\sigma_{\psi}$ from the resonances $\psi(3095)$ and $\psi(3684)$ were subtracted from the efficiency corrected cross sections. The same procedure was applied to total as well as inclusive cross sections at c.m. energies between 2.6 GeV and 7.8 GeV.

A. Total Hadronic Cross Section

The total cross section for the production of hadrons by one-photon annihilation is presented in Fig. 12 and Table II in form of the ratio to the cross section for the production of muon pairs, calculated in lowest order QED. The errors shown are purely statistical; in addition there are overall and point-to-point systematic errors. From a study of data taken at different times at the same c.m. energy, we estimated the systematic point-to-point errors to average ±3%. At energies above 6 GeV, the systematic uncertainty in the detection efficiency (± 8%), the luminosity measurement (± 6%), the event selection procedure (± 2%), and the background subtraction (±3%) yielded an overall systematic error of ±10%. From a study of the energy dependent detection efficiency with different Monte Carlo models and different parameters, and from the sensitivity to the measured TASH efficiency, we concluded that there was room for an additional smooth variation of the detection efficiency of 10% between the highest and the lowest c.m. energy. Thus the overall systematic error was estimated to be ±10% at energies above 6 GeV, increasing smoothly up to ±20% at 2.6 GeV.

We observe two regions where $R = \sigma_{HAD}/\sigma_{\mu\mu}$ is roughly independent of energy, and a transition region between them. Below 3.5 GeV, R is approximately constant with a value of 2.7 ± 0.5; above 5.5 GeV, the value is 4.3 ± 0.4. The errors quoted include statistical and systematic uncertainties.

In Fig. 13, the results of this experiment are compared with measurements from the PLUTO[29] and the DASP[30] experiments at DORIS. The Mark I data are also given in Table III. All errors are statistical only. The difference in structure, particularly above 4.0 GeV, is believed to be primarily due to differences in the treatment of radiative corrections. The Mark I data show a broad enhancement between 4.0 GeV and 4.2 GeV in addition to the resonances at 3.77 GeV[10] and 4.4 GeV.[23] Judging from the very sharp rise at 4.0 GeV, it appears that this enhancement could be more complicated than the simple broad peak that was assumed in the radiative correction (compare Fig. 8). Any structure gets enhanced by radiative corrections upon its inclusion in the shape of σ_0. Typically, in this region, a peak will be increased by 10% and a dip decreased by about the same amount. The DASP group inferred the existence of narrow Breit-Wigner resonances at 4.04 GeV and 4.16 GeV,[30] and consequently the corrected data look markedly different in detail. All three experiments observe a clear enhancement at 4.4 GeV, but differ as to its height and width. Again, this comparison is affected by differences in radiative corrections. Below 3.5 GeV and near 5 GeV, experiments agree to within ±10% on the value of R, well within quoted systematic errors.

A large fraction of the Mark I data consists of small samples of data recorded during short runs at c.m. energies spaced by a few MeV. The step size was chosen to be comparable to the energy spread of the beams, and resonances that are narrow compared to the energy resolution appeared as enhancements for several adjacent measurements, and the integrated cross section could be measured. During the very first systematic measurement of this kind, the $\psi(3684)$ was discovered.[8] Since then, the search has been extended to cover the whole energy range of the machine. No other narrow resonances were found. The data were used to set upper limits on the integrated cross section for the production of a narrow Breit-Wigner resonance by comparing the cross sections with the expected yields.[31] The results are given in Table IV in terms of 90% confidence limits for radiatively corrected integrated cross sections and for the leptonic width Γ_{ee}. For comparison, these limits are more than an order of magnitude smaller than the integrated cross sections for well-known vector mesons; for instance the $\psi(3684)$ has a value of roughly 3700 nb MeV.

B. Charged Particle Multiplicities

The multiplicity distribution is a very basic input to models of multi-hadron production in various types of particle interactions. The "unfold" procedure applied in this analysis results in a measurement of the produced charged particle multiplicity distribution. In Fig. 14, the partial cross section for hadronic events of a specific charged particle multiplicity is presented for multiplicities 2, 4, 6 and greater than 6. The data are plotted in terms of the fraction of the total cross section, as a function of the c.m. energy. Only statistical errors are given; the systematic errors are larger than for the total cross section because the fractions f_p depend sensitively on the number of detected events at each multiplicity and are highly correlated. By varying the production model and the unfold parameters, the overall systematic uncertainty was estimated to drop from 25% at 2.6 GeV c.m. energy to 15% at 6 GeV and above. Point-to-point errors averaged ±5%. These cross sections vary smoothly over the whole c.m. energy range covered, with no explicit structure near 4 GeV, indicating that the rapid change in the total cross section is not associated with a drastic change in charged particle multiplicity. This observation is supported by a comparison of charged particle multiplicities at four selected c.m. energies, as given in Fig. 15. While the constraints of phase space limit the particle multiplicity at the lower energies, this restriction becomes considerably less above 6 GeV. This effect is reproduced qualitatively by the Monte Carlo simulation. For efficiency measurements, the quantitative differences between the data and the Monte Carlo are corrected for by the unfold procedure.

The average charged particle multiplicity, $\langle n_{CH} \rangle$, versus the c.m. energy is presented in Fig. 16 and in Table V. The observed energy dependence of the Mark I data is consistent with a logarithmic increase, well represented by

$$\langle n_{CH} \rangle = a + b \ln s \quad , \qquad (6.2)$$

where a = 2.1 and b = 0.84, and s is in units of GeV^2. Obviously, some other functions describing a slow increase cannot be ruled out. The overall behavior is reminiscent of multiplicity growth in many hadronic experiments at comparable energies.[35]

In summary, there is no evidence for abrupt changes in the multiplicity distributions for charged particles in the transition region near 4 GeV, though experimental uncertainties are not small and could obscure some important changes in dynamics. The efficiency calculations at various energies are based on the jet model and do not include exclusive two-body reactions that dominate charmed hadron production near threshold. Consequently, possible changes near 4 GeV may have been underestimated.

C. Inclusive Momentum Spectra

Inclusive momentum spectra of charged particles were measured at several different c.m. energies. The results are presented in terms of the differential cross section $s\,d\sigma/dx$ in Fig. 17, where the variable $x = 2p/E_{c.m.}$ is computed from the particle momentum rather than its energy because mass identification was not available over the whole momentum range. In this measurement pions from K^o decay entered as two particles, and corrections have been applied for electrons from photon conversion and Dalitz pairs. These measurements of single hadron spectra were subject to larger systematic errors than the total cross section measurement. However, for comparisons of inclusive distributions measured at different c.m. energies, the sensitivity to the production model, the detector efficiency, and the overall normalization is much less critical.

The spectra for all five c.m. energies shown in Fig. 17 rise sharply at small values of x, peak near $x = 0.2$, and then fall with increasing x. Above $x = 0.5$, the spectra agree to within experimental errors, and can be well approximated by an exponential function of the form $f(x) = ce^{-bx}$ with $b = 6.8 \pm 0.3$, where the stated error includes systematic uncertainties. A detailed comparison of the data recorded between 4 GeV and 5 GeV and above 6 GeV, shows an enhancement of lower energy data in the range of $0.2 < x < 0.4$ relative to the higher energy data. This is illustrated in Fig. 17b. The observed effect is expected from the production of pairs of charmed particles near threshold.

The inclusive momentum spectra at 4.8 GeV and 7.4 GeV are compared in Fig. 18 with previously published measurements from the PLUTO[33] and

DASP[36] experiments at 5 GeV c.m. energy. Given the uncertainty in the overall normalization and detection efficiencies for different experiments, as well as the difference in the measured charged particle multiplicities, the observed differences are not surprising.

In order to investigate the energy dependence more critically, we plotted the cross section $s\,d\sigma/dx$ versus $E_{c.m.}$ for several x intervals in Fig. 19. Bjorken[12] scaling implies that $s\,d\sigma/dx$ should not change with c.m. energy at fixed values of x. At low x and $s = E^2_{c.m.}$, scaling is not expected to hold because effects of particle masses are not negligible. The scale breaking between 4 GeV and 5 GeV for x less than 0.5 can be attributed to the threshold for the pair production of charmed particles. This is supported by measurements of inclusive K^0 production in this energy range[37] as well as by the observation of exclusive production of charmed meson pairs.[38] Excluding the charm threshold region, the data are independent of $E_{c.m.}$ over the entire energy range studied for $x \geq 0.4$. This scaling behavior is quite remarkable in light of the increase in R and suggests that the increase is confined to relatively small values of x. Another way to arrive at the same conclusion is via the sum rule,

$$\frac{1}{\sigma_{\mu\mu}} \int \frac{d\sigma}{dx}\, dx = \langle n_{CH} \rangle R \quad . \tag{6.3}$$

Since the average charged particle multiplicity rises approximately logarithmically with increasing c.m. energy, the integral over x must also increase. This increase is, however, restricted to small values of x, where scaling is broken. The differential cross section measurement $s\,d\sigma/dx$ is compared with the measurements of $R = \sigma_{HAD}/\sigma_{\mu\mu}$

and the charged multiplicity $\langle n_{CH} \rangle$ using the sum rules stated above. The extrapolation to zero momentum was made by comparison to Monte Carlo simulated data. The results, presented in Table VI, agree reasonably well.

VII. CONCLUSIONS

In this article we have reported measurements of hadron production by e^+e^- annihilation at energies between 2.6 GeV and 7.8 GeV. The total hadronic cross section scales in two different energy regions. For c.m. energies below 3.7 GeV the ratio $R = \sigma_{HAD}/\sigma_{\mu\mu}$ has a constant value of 2.7 ± 0.5, while R is 4.3 ± 0.4 between 5.0 GeV and 7.8 GeV. A transition with distinct Breit-Wigner resonances at 3.77 GeV and 4.4 GeV and additional, more complicated structure connects these two scaling regions. Aside from the narrow resonances, $\psi(3095)$ and $\psi(3684)$, no additional narrow resonances have been found. Upper limits of less than 1 keV have been set for leptonic widths of narrow vector meson states. The mean charged particle multiplicity increases slowly with energy, from 3.8 ± 0.3 at 2.8 GeV to 5.5 ± 0.2 at 7.4 GeV, and is consistent with the Feynman scaling hypothesis.[39] Single particle inclusive momentum spectra exhibit Bjorken scaling for $x > 0.4$ over the entire energy range of the experiment, with the exception of the transition region from 3.7 GeV to 5 GeV.

All these features of hadron production by e^+e^- colliding beams are natural consequences of the quark-parton model and are well described qualitatively. In the context of this model, it follows from Eq. (1.1) that new partons must be coming into play near 4 GeV to effect the increase in R. In the low energy scaling region, the model predicts $R = 2$ for nine quarks arranged in three flavors and three colors.

The upward step of 1.6 ± 0.3 is roughly 15% larger than the value of 4/3 expected for the charmed quark of charge 2/3, and the value of R for energies above 5 GeV exceeds the naive quark model prediction of 10/3 by more than two standard deviations.

The predictions of the naive quark-parton model are identical to those of QCD, in lowest order perturbation theory. According to QCD, the produced quarks radiate gluons, which like the quarks are expected to materilize as hadrons in the final state. The ratio R takes the form[40]

$$R = 3\sum_q e_q^2 \left\{ 1 + \frac{\alpha_s(s)}{\pi} + C_2 \left(\frac{\alpha_s(s)}{\pi} \right)^2 + \ldots \right\} \quad . \qquad (7.1)$$

The QCD corrections are expressed in terms of a small coupling constant $\alpha_s(s)$ that decreases logarithmically with s $[\alpha_s(s) \sim (\log s/\Lambda^2)^{-1}]$ and depends on the scale parameter Λ. The coefficient C_2 can be calculated[41] and is of order one. While at high energies R is quite insensitive to the value of Λ, there is a measureable difference between the predictions of QCD and the naive quark-parton model at lower energies.

In Fig. 20, the existing measurements of R,[42,43] including recent results from PETRA,[44] are compared with QCD calculations by Barnett et al.[45] for several values of Λ. $\Lambda = 0$ corresponds to the quark-parton model prediction with $\alpha_s = 0$. The agreement between the data and the QCD predictions is satisfactory only above 10 GeV, but rather marginal for energies below. A variety of explanations for this apparent discrepancy have been considered, most of which seem to be neither plausible nor appealing. While the numerical parameters which enter into QCD calculation, like the scale parameter Λ and the quark masses, are only approximately known, they cannot change the calculated cross sections substantially. From deep inelastic scattering experiments Λ may not be known to better than ~200 MeV (with a value of probably less than 400 MeV), leading to an uncertainty in R of roughly 2% for $\sqrt{s}$ near 6 GeV. The contribution due to the uncertainty in the charmed-quark mass may be as large as 10% near threshold but it is believed to be far less than 1% above 5 GeV. On the other hand, nonperturbative effects due to hadronization could be important, particularly near thresholds for new, exclusive channels. Several authors[45,46] have applied dispersion relations, local duality, and different smearing techniques to estimate the threshold behavior of the total cross section. None of these calculations provides a satisfactory explanation for the measured values of R between 5 GeV and 7 GeV, and this precludes a straight-forward interpretation of the measurement in terms of the coupling constant $\alpha_s(s)$ in this energy region.

In QCD the s dependence of the coupling constant $\alpha_s(s)$ affects the scaling behavior of the inclusive momentum distributions $s\,d\sigma/dx$, but these effects are small and vary only logarithmically with s. The limited c.m. energy range covered by this experiment, the sizable systematic errors and the presence of the charmed particle threshold do not allow for quantitative tests of this prediction. Qualitatively, the observed scaling behavior of the inclusive momentum spectra and the energy independence of R above 5 GeV support the quark-parton hypothesis.

REFERENCES

1. $\mu\pi$ group: F. Ceradini et al., Phys. Lett. 47B, 80 (1973).

   $\gamma\gamma$ group: C. Bacci et al., Phys. Lett. 44B, 533 (1973).

   Boson group: B. Bartoli et al., Phys. Rev. D6, 2374 (1972).

   BCF group: M. Bernardini et al., Phys. Lett. 51B, 200 (1974).

2. G. Cosme et al., Phys. Lett. 40B, 685 (1972).

3. L. M. Kurdadze et al., Phys. Lett. 42B, 515 (1972).

4. A. Litke et al., Phys. Rev. Lett. 30, 1189 (1973); ibid., 1349 (1973).

   G. Tarnopolský et al., Phys. Rev. Lett. 32, 432 (1974).

5. S. D. Drell, D. J. Levy and T. M. Yan, Phys. Rev. 187, 2159 (1969).

6. N. Cabibbo et al., Nuovo Cimento Lett. 4, 35 (1970).

7. M. Spinetti, Proceedings of the International Symposium on Lepton and Photon Interactions at High Energies, Fermilab (1979), p. 506; V. A. Siderov, ibid., p. 490.

8. J.-E. Augustin et al., Phys. Rev. Lett. 33, 1406 (1974);

   J. J. Aubert et al., Phys. Rev. Lett. 33, 1404 (1974).

9. G. S. Abrams et al., Phys. Rev. Lett. 33, 1453 (1974).

10. P. A. Rapidis et al., Phys. Rev. Lett. 39, 526 (1977);

    W. Bacino et al., Phys. Rev. Lett. 40, 671 (1978).

11. Y. S. Tsai, Phys. Rev. D12, 3533 (1976).

12. J. D. Bjorken, Phys. Rev. 179, 1547 (1969).

13. This report is based on the analysis of J. Siegrist, Ph.D. thesis, SLAC-Report 225 (1979).

14. G. Hanson et al., Phys. Rev. D (following paper).

15. SPEAR Storage Ring Group, M. Allen et al., IXth International Conference on High Energy Accelerators, Stanford (1974).

16. J. S. Whitaker, Ph.D. thesis, LBL Report LBL-5518 (1976).

17. R. J. Hollebeek, Ph.D. thesis, LBL Report LBL-3874 (1975).

18. M. L. Perl, Annu. Rev. Nucl. Part. Sci. 30, 299 (1980); G. Flügge, Z. Phys. C1, 121 (1979).

19. The computer program used was SAGE. J. H. Friedman, J. Comput. Phys. 7, (1971) and R. B. Chaffee, "A User's Guide for SAGE," SLAC Computational Group, Note 195 (1979), unpublished.

20. The computer program used was GENIUS, based on (and coded by) D. C. Carey and D. Drijard, J. Comput. Phys. 28, 327 (1978).

21. G. Bonneau and F. Martin, Nucl. Phys. B27, 381 (1971).

22. Cubic polynomials ("splines") were joined with continuous firs and second derivatives.

23. J. Siegrist et al., Phys. Rev. Lett. 36, 700 (1976).

24. P. Rapidis et al., Phys. Rev. Lett. 39, 526 (1977); ibid., 39, 974 (1977).

25. J. D. Jackson and D. L. Scharre, Nucl. Instrum. Methods 128, 13 (1975).

26. A. M. Boyarski et al., Phys. Rev. Lett. 34, 1357 (1975); V. Lüth et al., Phys. Rev. Lett. 35, 1124 (1975).

27. F. A. Berends et al., Nucl. Phys. B68, 541 (1974); ibid., B63, 381 (1973).

28. J.-E. Augustin et al., Phys. Rev. Lett. 34, 233 (1975).

29. J. Burmeister et al., Phys. Lett. 66B, 395 (1977).

30. R. Brandelik et al., Phys. Lett. 76B, 361 (1978).

31. A. M. Boyarski et al., Phys. Rev. Lett. 34, 762 (1975).

32. C. Bacci et al., Phys. Lett. 88B, 234 (1979);

E. Esposito, Nuovo Cimento Lett. 19, 21 (1977).

33. A. Bäcker, Dissertation, DESY Internal Report F33-77/03, unpublished.

34. R. Brandelik et al., Nucl. Phys. B148, 189 (1979).

35. J. Whitmore, Phys. Rep. C10, 273 (1974);

M. Basile et al., Phys. Lett. 95B, 311 (1980).

36. R. Brandelik et al., Phys. Lett. 67B, 358 (1977).

37. V. Lüth et al., Phys. Lett. 70B, 120 (1977).

38. G. Goldhaber et al., Phys. Lett. 69B, 503 (1977).

39. R. P. Feynman, Phys. Rev. Lett. 23, 1415 (1969).

40. T. Appelquist and H. Georgi, Phys. Rev. D8, 4000 (1973);

A. Zee, Phys. Rev. D8, 4038 (1973).

41. E. G. Floratos et al., Phys. Lett. 80B, 269 (1979);

W. A. Bardeen and A. J. Buras, Phys. Lett. 86B,61 (1979).

42. J. Kirkby, invited talk presented at the 1979 International Symposium on Lepton and Photon Interactions at High Energies, Batavia (1979).

43. E. Bloom et al., SLAC-PUB-2779 (1981), XVIth Rencontre de Moriond, Les Arcs, France (1981).

44. R. Felst, invited talk presented at the 1981 International Symposium on Lepton and Photon Interactions at High Energies, Bonn (1981).

45. R. M. Barnett, M. Dine and L. McLerran, Phys. Rev. D22, 594 (1980). In this calculation, mass dependent terms in the running coupling constant have been included for the charm and heavier quarks.

46. T. Appelquist and H. Georgi, Phys. Rev. D12, 1404 (1975);

E. C. Poggio, H. R. Quinn and S. Weinberg, Phys. Rev. D13, 1958 (1976); R. Shanker, Phys. Rev. D15, 755 (1978).

TABLE I

Components of the detector, dimensions and the amount of material they represent.

Item	Average radius (cm)	Fraction of 4π Acceptance	Length (z) (cm)	Thick-ness (cm)	Fraction of Radiation Length	Fraction of Absorption Length
Beampipe	8.0	-	-	0.0273	0.016	0.002
Pipe Counters	12.0	0.83	90	1.37	0.033	0.020
MWPC1	17.3	0.82	± 25	1.98	0.0066	-
MWPC2	22.4	0.88	± 41	1.98	0.0066	-
WSC1	66	0.86	± 110	3.8	0.0017	0.001
WSC2	91	0.77	± 110	3.8	0.0017	0.001
WSC3	112	0.73	± 120	3.8	0.0017	0.001
WSC4	135	0.71	± 134	3.8	0.0017	0.001
TOF Counters	152.4	0.65	± 130	2.5	0.060	0.037
Coil	166.4	0.74	± 182.9	11.0	1.0	0.24
Shower Counters	178.4	0.66	± 155	13.0	5.79	0.22
Flux Return	211	-	± 183	20.0	11.4	1.17
Muon WSC	219	0.73	± 234	5.7	0.22	0.07

TABLE II

Measurements of $R = \sigma_{HAD}/\sigma_{\mu\mu}$ versus the c.m. energy $E_{c.m.}$ (in GeV) (as presented in Figure 12).

$E_{c.m.}$	R	$E_{c.m.}$	R	$E_{c.m.}$	R	$E_{c.m.}$	R
2.60	2.84 ± 0.74	4.10	4.97 ± 0.15	5.60	4.08 ± 0.32	6.60	4.50 ± 0.17
2.80	2.54 ± 0.46	4.15	4.78 ± 0.13	5.70	4.09 ± 0.16	6.65	4.25 ± 0.16
3.00	2.59 ± 0.15	4.20	4.11 ± 0.14	5.75	4.12 ± 0.20	6.70	4.63 ± 0.15
3.15	2.79 ± 0.42	4.25	3.78 ± 0.18	5.80	4.13 ± 0.16	6.75	4.38 ± 0.15
3.20	2.80 ± 0.32	4.30	3.47 ± 0.15	5.85	4.13 ± 0.19	6.80	4.44 ± 0.16
3.30	2.65 ± 0.46	4.35	3.91 ± 0.19	5.90	4.09 ± 0.14	6.85	4.50 ± 0.13
3.40	2.35 ± 0.28	4.40	5.01 ± 0.08	5.95	4.17 ± 0.16	6.90	4.41 ± 0.15
3.45	2.12 ± 0.30	4.45	4.60 ± 0.18	6.00	4.17 ± 0.09	6.95	4.23 ± 0.17
3.50	2.63 ± 0.35	4.50	3.79 ± 0.18	6.05	4.16 ± 0.18	7.00	4.10 ± 0.12
3.55	2.50 ± 0.30	4.55	3.55 ± 0.25	6.10	4.04 ± 0.15	7.05	4.31 ± 0.09
3.60	2.82 ± 0.26	4.60	3.33 ± 0.19	6.15	4.34 ± 0.16	7.10	4.32 ± 0.14
3.65	2.50 ± 0.19	4.65	3.64 ± 0.53	6.20	4.05 ± 0.08	7.15	4.29 ± 0.11
3.75	4.08 ± 0.36	4.70	3.86 ± 0.23	6.25	3.96 ± 0.14	7.20	4.27 ± 0.11
3.80	2.76 ± 0.26	4.80	3.97 ± 0.19	6.30	4.27 ± 0.14	7.25	4.39 ± 0.11
3.85	2.40 ± 0.29	4.90	3.61 ± 0.25	6.35	4.47 ± 0.17	7.30	4.29 ± 0.11
3.90	3.04 ± 0.13	5.10	4.34 ± 0.29	6.40	4.31 ± 0.13	7.35	4.33 ± 0.09
3.95	4.07 ± 0.20	5.20	3.57 ± 0.27	6.45	4.23 ± 0.14	7.40	4.46 ± 0.08
4.00	4.29 ± 0.13	5.30	3.68 ± 0.27	6.50	4.40 ± 0.15	7.45	4.51 ± 0.14
4.05	5.73 ± 0.09	5.40	4.24 ± 0.31	6.55	4.66 ± 0.16	7.50	4.18 ± 0.59
		5.50	3.57 ± 0.24			7.80	4.47 ± 0.53

TABLE III

Measurements of R = $\sigma_{HAD}/\sigma_{\mu\mu}$ versus the c.m. energy $E_{c.m.}$ (in GeV) (as presented in Figure 13c).

$E_{c.m.}$	R	$E_{c.m.}$	R	$E_{c.m.}$	R	$E_{c.m.}$	R
3.40	1.64 ± 0.58	3.67	2.37 ± 0.39	3.98	4.11 ± 0.33	4.25	2.99 ± 0.47
3.41	3.12 ± 0.88	3.72	3.12 ± 0.94	3.99	4.04 ± 0.19	4.26	4.71 ± 0.63
3.42	1.89 ± 0.64	3.73	2.83 ± 0.88	4.00	3.94 ± 0.22	4.27	3.52 ± 0.27
3.43	1.24 ± 0.65	3.74	4.78 ± 1.16	4.01	4.47 ± 0.36	4.28	3.56 ± 0.31
3.44	2.05 ± 0.67	3.75	4.80 ± 1.37	4.02	5.16 ± 0.30	4.29	3.42 ± 0.17
3.45	2.59 ± 0.65	3.76	4.01 ± 0.51	4.03	5.77 ± 0.10	4.30	3.62 ± 0.50
3.46	2.70 ± 0.84	3.77	4.38 ± 0.84	4.04	5.21 ± 0.25	4.33	3.45 ± 0.26
3.47	2.01 ± 0.60	3.78	4.05 ± 0.69	4.05	4.88 ± 0.50	4.35	3.96 ± 0.38
3.48	2.69 ± 0.84	3.79	3.52 ± 0.55	4.06	4.75 ± 0.27	4.37	4.46 ± 0.34
3.49	4.20 ± 1.20	3.80	1.46 ± 0.41	4.07	4.73 ± 0.59	4.38	4.67 ± 0.38
3.50	1.27 ± 0.49	3.81	2.78 ± 0.84	4.08	5.29 ± 0.40	4.39	4.19 ± 0.21
3.51	2.69 ± 0.74	3.82	1.47 ± 0.45	4.09	4.79 ± 0.22	4.40	5.26 ± 0.34
3.52	2.87 ± 0.76	3.83	1.89 ± 0.57	4.10	5.17 ± 0.56	4.41	5.06 ± 0.10
3.53	1.77 ± 0.55	3.84	2.42 ± 0.68	4.11	4.97 ± 0.21	4.42	5.17 ± 0.09
3.54	2.75 ± 0.85	3.85	2.52 ± 0.61	4.12	5.39 ± 0.72	4.43	5.08 ± 0.30
3.55	2.80 ± 0.64	3.86	2.62 ± 0.72	4.13	4.47 ± 0.42	4.44	4.26 ± 0.28
3.56	2.59 ± 0.59	3.87	2.66 ± 0.64	4.14	4.83 ± 0.14	4.45	4.59 ± 0.49
3.57	2.62 ± 0.84	3.88	2.40 ± 0.70	4.15	4.72 ± 0.59	4.46	4.63 ± 0.53
3.58	2.01 ± 0.60	3.89	2.83 ± 0.17	4.16	5.22 ± 0.80	4.47	4.58 ± 0.62
3.59	2.87 ± 0.59	3.90	2.98 ± 0.28	4.17	4.79 ± 0.53	4.49	3.61 ± 0.22
3.60	2.56 ± 0.74	3.91	3.21 ± 0.34	4.18	5.20 ± 0.58	4.51	4.13 ± 0.31
3.61	3.38 ± 0.86	3.92	3.49 ± 0.30	4.19	4.08 ± 0.17	4.53	3.64 ± 0.38
3.62	3.70 ± 1.01	3.93	4.27 ± 0.49	4.20	3.85 ± 0.63	4.54	3.47 ± 0.34
3.63	2.60 ± 0.52	3.94	3.50 ± 0.33	4.21	3.99 ± 0.32	4.58	3.69 ± 0.57
3.64	2.18 ± 0.31	3.95	4.04 ± 0.51	4.22	3.93 ± 0.53	4.59	3.26 ± 0.20
3.65	2.82 ± 0.49	3.96	4.27 ± 0.38	4.23	4.16 ± 0.57	4.63	3.59 ± 0.52
3.66	2.78 ± 0.43	3.97	4.61 ± 0.53	4.24	3.92 ± 0.32	4.68	3.93 ± 0.36
						4.69	3.77 ± 0.29

TABLE IV

Search for narrow resonances with masses between 3.2 and 7.45 GeV. Upper limits (90% confidence level) for the radiatively corrected integrated cross section and for the leptonic width Γ_{ee} at a possible narrow resonance with spin J = 1. The width of this resonance was assumed to be small compared to the mass resolution.

Mass Range (GeV)	$\int \sigma_{HAD}\, dE_{c.m.}$ (nb MeV)	Γ_{ee} (keV)
3.2 → 3.50	970	0.47
3.50 → 3.68	780	0.44
3.72 → 4.00	850	0.55
4.00 → 4.40	620	0.47
4.40 → 4.90	580	0.54
4.90 → 5.65	800	0.97
5.65 → 6.00	90	0.13
6.00 → 6.45	100	0.17
6.45 → 6.95	65	0.13
6.95 → 7.45	35	0.07

TABLE V

The mean charged particle multiplicity versus the c.m. energy $E_{c.m.}$ (as presented in Figure 16).

$E_{c.m.}$ (GeV)	Mean Charged Multiplicity	$E_{c.m.}$ (GeV)	Mean Charged Multiplicity
2.60	3.75 ± 0.42	5.40	5.15 ± 0.25
2.80	3.79 ± 0.24	5.60	4.96 ± 0.18
3.00	3.93 ± 0.09	5.80	5.28 ± 0.13
3.20	4.19 ± 0.15	6.00	4.97 ± 0.11
3.30	4.14 ± 0.25	6.10	5.09 ± 0.16
3.40	4.10 ± 0.22	6.20	5.32 ± 0.10
3.60	4.44 ± 0.25	6.30	5.33 ± 0.16
3.80	4.29 ± 0.06	6.40	5.33 ± 0.16
3.90	4.32 ± 0.13	6.50	5.32 ± 0.19
4.00	4.37 ± 0.04	6.60	5.02 ± 0.18
4.10	4.40 ± 0.10	6.70	5.20 ± 0.17
4.20	4.58 ± 0.13	6.80	5.27 ± 0.13
4.30	4.61 ± 0.15	6.90	5.27 ± 0.19
4.40	4.56 ± 0.04	7.00	5.15 ± 0.14
4.50	4.79 ± 0.23	7.10	5.28 ± 0.15
4.60	4.98 ± 0.30	7.20	5.29 ± 0.11
4.70	4.49 ± 0.30	7.30	5.30 ± 0.13
4.80	4.85 ± 0.07	7.40	5.49 ± 0.14
5.10	4.43 ± 0.23	7.80	5.75 ± 0.33

TABLE VI

Comparison of the average charged particle multiplicity at various c.m. energies with the inclusive charged particle momentum spectra using the sum rule in Equation (6.3).

$E_{c.m.}$	$\frac{1}{R}\frac{3}{4\pi\alpha^2}\int s\frac{d\sigma}{dx}\,dx$	$\langle n_{ch} \rangle$
3.0	3.7 ± 0.2	3.9 ± 0.1
4.8	5.5 ± 0.2	4.9 ± 0.1
6.2	5.9 ± 0.3	5.3 ± 0.2
7.4	5.9 ± 0.3	5.5 ± 0.2

FIGURE CAPTIONS

Fig. 1. Earlier measurements of the ratio $R = \sigma_{HAD}/\sigma_{\mu\mu}$ as a function of the c.m. energy $E_{c.m.}$ from Frascati (ADONE),[1] Orsay (ACO),[2] Novosibirsk (VEPP-2)[3] and Cambridge (CEA).[4]

Fig. 2. Endview of the solenoidal magnetic detector MARK I.

Fig. 3. Sectional view of the detector. The positron beam entered from the right, the electron beam from the left.

Fig. 4. The efficiency of the TASH coincidence for a single charged hadron as a function of its momentum. The dashed line marks the level of accidental coincidences.

Fig. 5. Position of the vertex for multiprong events:

a) radial distance R from the beam line,

b) longitudinal position relative to the interaction point, for events with $R < 4$ cm. The arrows mark the cuts for the hadronic event selection.

Fig. 6. Detection efficiency matrix elements $\tilde{\varepsilon}_{0p}$ versus the c.m. energy $E_{c.m.}$, where $\tilde{\varepsilon}_{0p}$ is the probability that an event produced with p charged particles is not detected.

Fig. 7. The yield of hadronic events corrected for detection efficiency, but not for radiative effects, and normalized to the cross section for muon-pair production.

Fig. 8′. Smoothed representation of the ratio $R_0 = \sigma_0/\sigma_{\mu\mu}$ used in calculating radiative correction [Equation (4.6)].

Fig. 9. Radiative corrections to the detection efficiency;

a) the curves represent the function $\tilde{\Omega}_p$, while points are Monte Carlo results for $\Omega_2 = \tilde{\Omega}_2\omega$, which reflect the shape of the cross section σ_0;

b) the multiplicity independent function ω.

Fig. 10. The average detection efficiency for hadronic events versus the c.m. energy $E_{c.m.}$. The line represents a smooth fit and was used for interpolation.

Fig. 11. The inclusive detection efficiency for a single charged hadron as a function of the scaled momentum $x = 2p/E_{c.m.}$ for c.m. energies of 3.0 GeV, 4.8 GeV and 7.4 GeV.

Fig. 12. The ratio $R = \sigma_{HAD}/\sigma_{\mu\mu}$ versus the c.m. energy $E_{c.m.}$.

Fig. 13. The ratio $R = \sigma_{HAD}/\sigma_{\mu\mu}$ in the c.m. energy range from 3.4 GeV to 5.5 GeV for three different experiments:

a) PLUTO[29]

b) DASP[30]

c) Mark I (this experiment).

All errors are statistical only.

Fig. 14. The ratio of the partial to the total hadron cross section, $f_p = \sigma_p/\sigma_{HAD}$ versus c.m. energy (σ_p refers to the cross section for the production of a hadronic state with p charged particles).

Fig. 15. Charged particle multiplicity distributions for various selected c.m. energies. The histograms indicate the distribution for the Monte Carlo simulation.

Fig. 16. The mean charged particle multiplicity as a function of the c.m. energy, data from SPEAR, ADONE[32] and DORIS.[33,34]

Fig. 17. Inclusive single charged particle momentum distribution, $x = 2p/E_{c.m.}$, for selected c.m. energies. The errors shown are purely statistical.

Fig. 18. A comparison between results from Mark I, PLUTO[30] and DASP[33] on the inclusive momentum distribution for c.m. energies between 4.8 GeV and 7.4 GeV. All errors indicated are statistical only.

Fig. 19. Test on scaling in the inclusive momentum distribution, $s\,d\sigma/dx$. All errors are statistical, but for this comparison of data at different energies systematic errors in the normalization and the detection efficiency are much less important.

Fig. 20. Comparison between measurements of R and QCD estimates[45] for several values of Λ (measured in GeV). In addition to the Mark I results, data from DELCO,[42] the Crystal Ball experiment,[43] DASP,[30] PLUTO,[29] and recent results from experiments at PETRA[44] are shown. The errors given are statistical, 10-15% systematic uncertainties are to be added. The location of the narrow resonances is indicated.

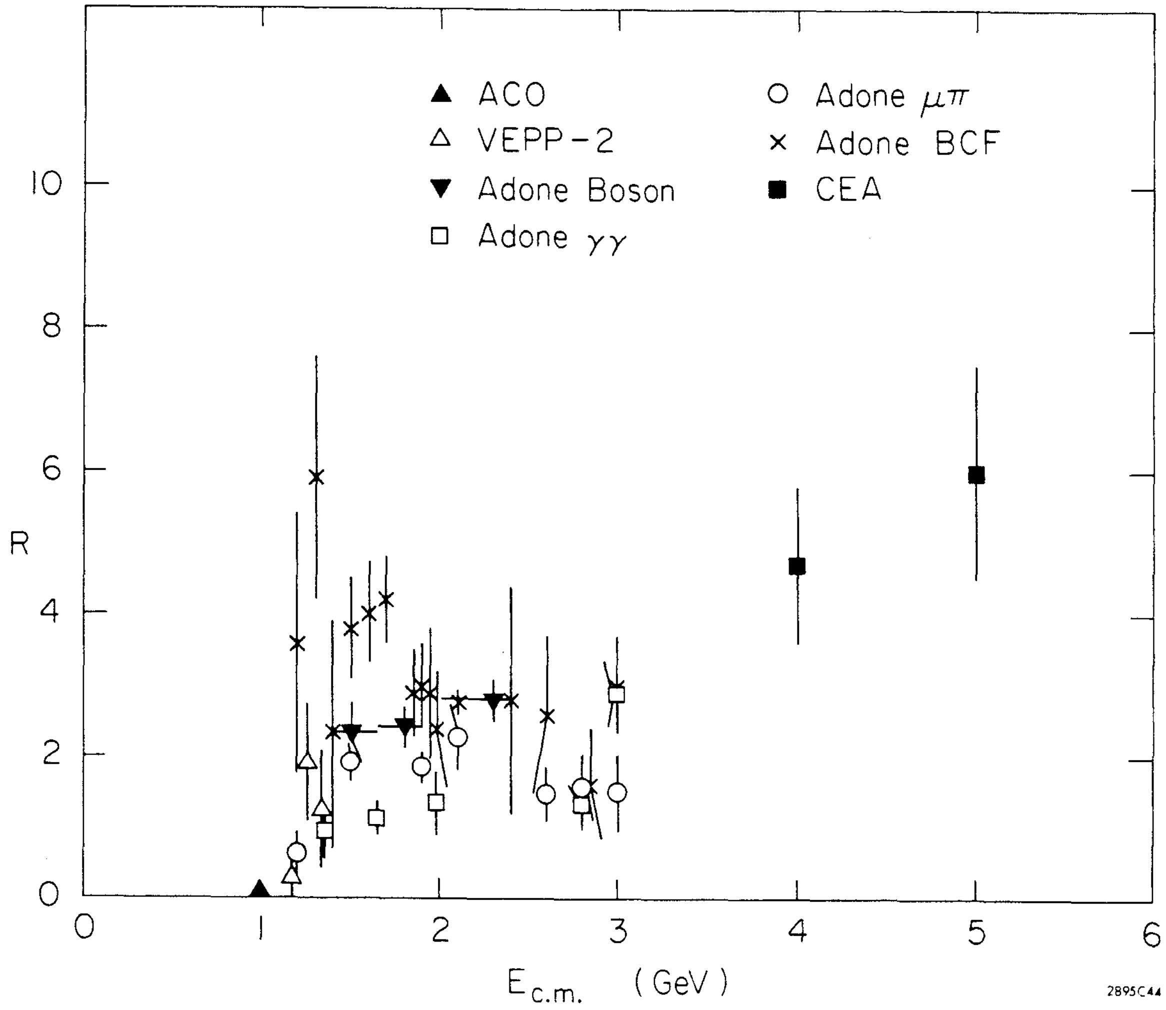
▲ ACO
△ VEPP-2
▼ Adone Boson
□ Adone $\gamma\gamma$
○ Adone $\mu\pi$
× Adone BCF
■ CEA
R
0
2
4
6
8
10
0
1
2
3
4
5
6
$E_{c.m.}$ (GeV)
2895C44

Fig. 1

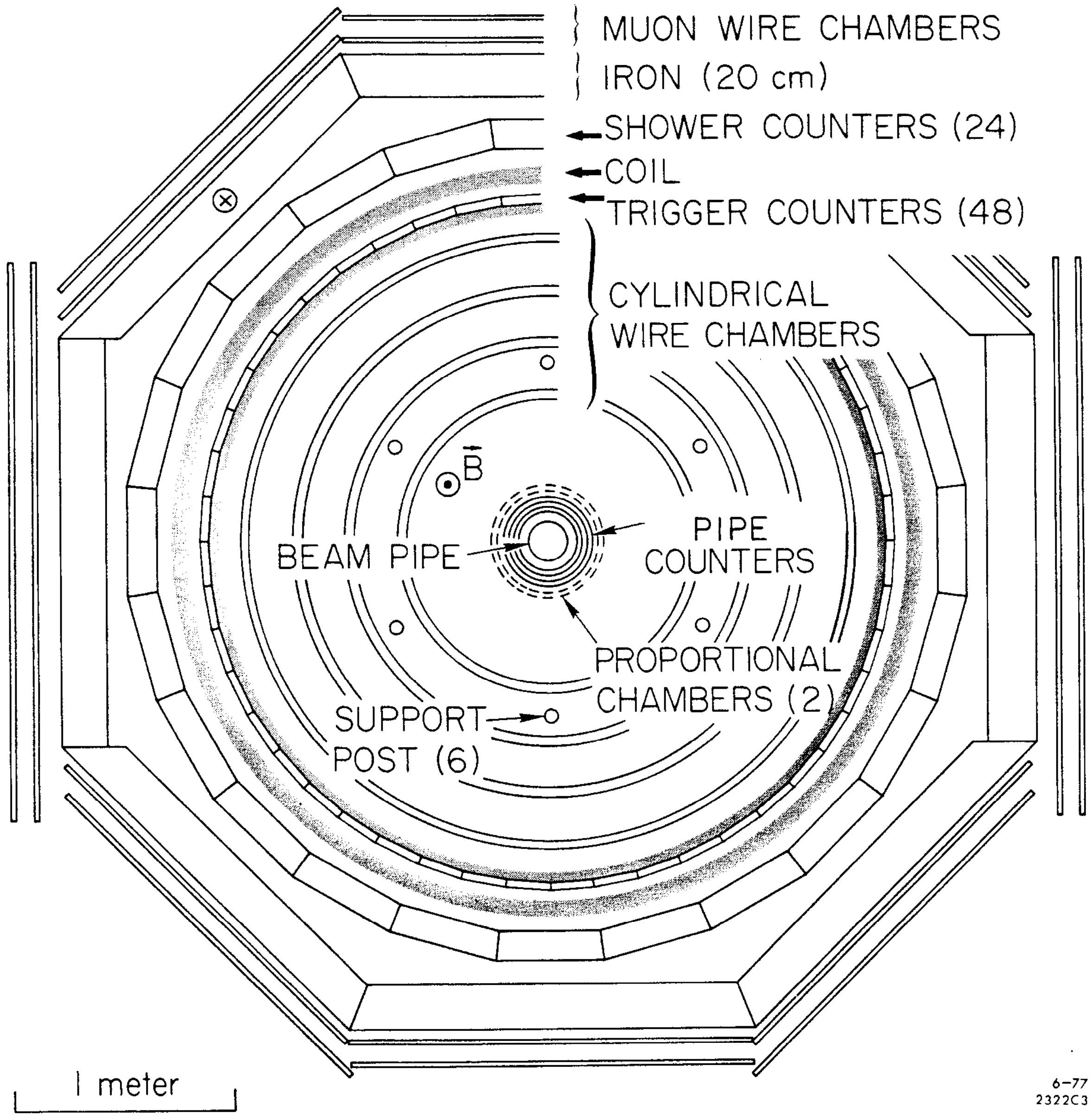
MUON WIRE CHAMBERS
IRON (20 cm)
SHOWER COUNTERS (24)
COIL
TRIGGER COUNTERS (48)
CYLINDRICAL WIRE CHAMBERS
B
PIPE COUNTERS
BEAM PIPE
PROPORTIONAL CHAMBERS (2)
SUPPORT POST (6)
1 meter
6-77
2322C3

Fig. 2

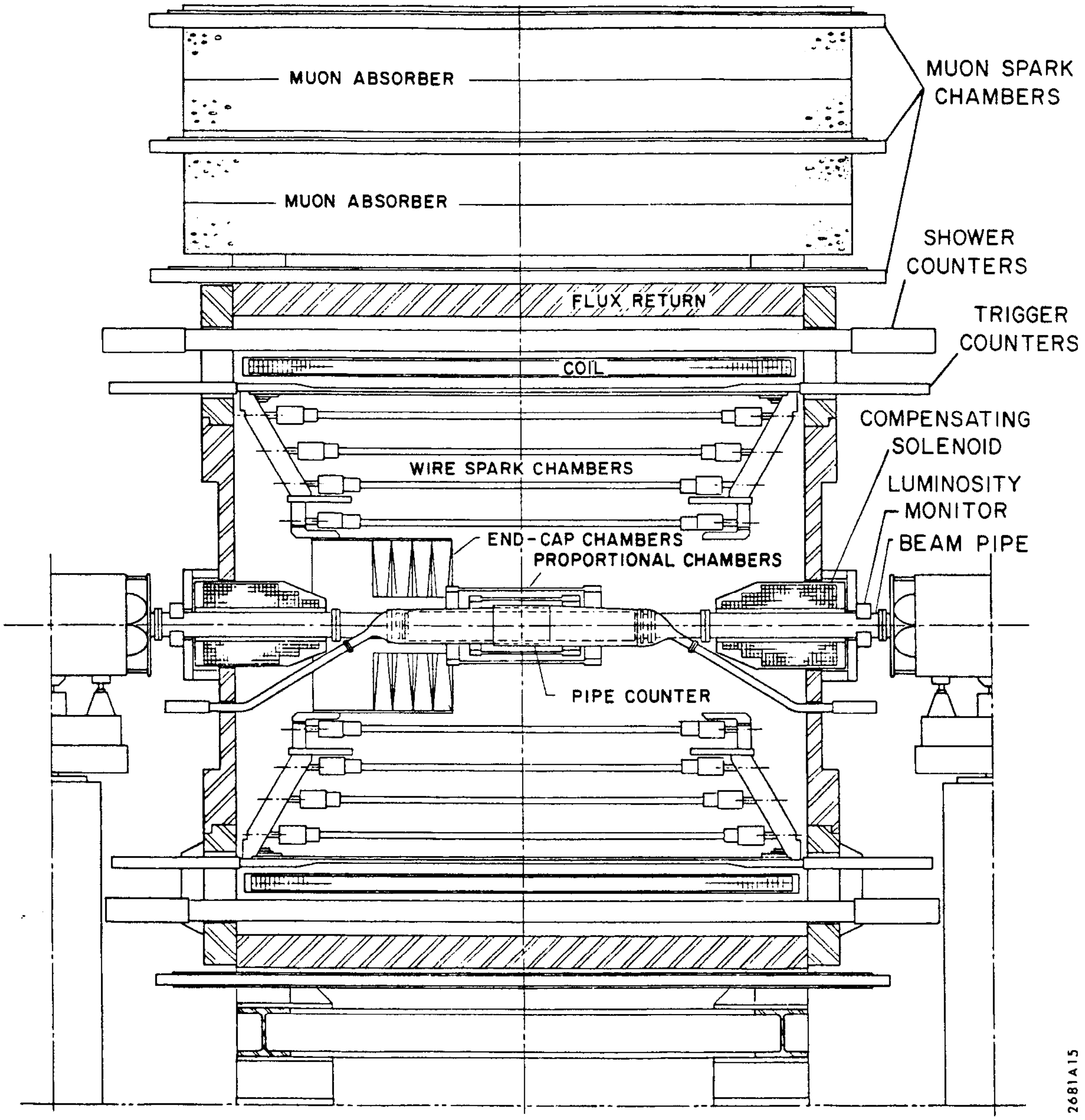
MUON SPARK CHAMBERS
MUON ABSORBER
MUON ABSORBER
SHOWER COUNTERS
FLUX RETURN
TRIGGER COUNTERS
COIL
COMPENSATING SOLENOID
WIRE SPARK CHAMBERS
LUMINOSITY MONITOR
END-CAP CHAMBERS
PROPORTIONAL CHAMBERS
BEAM PIPE
PIPE COUNTER
2681A15

Fig. 3

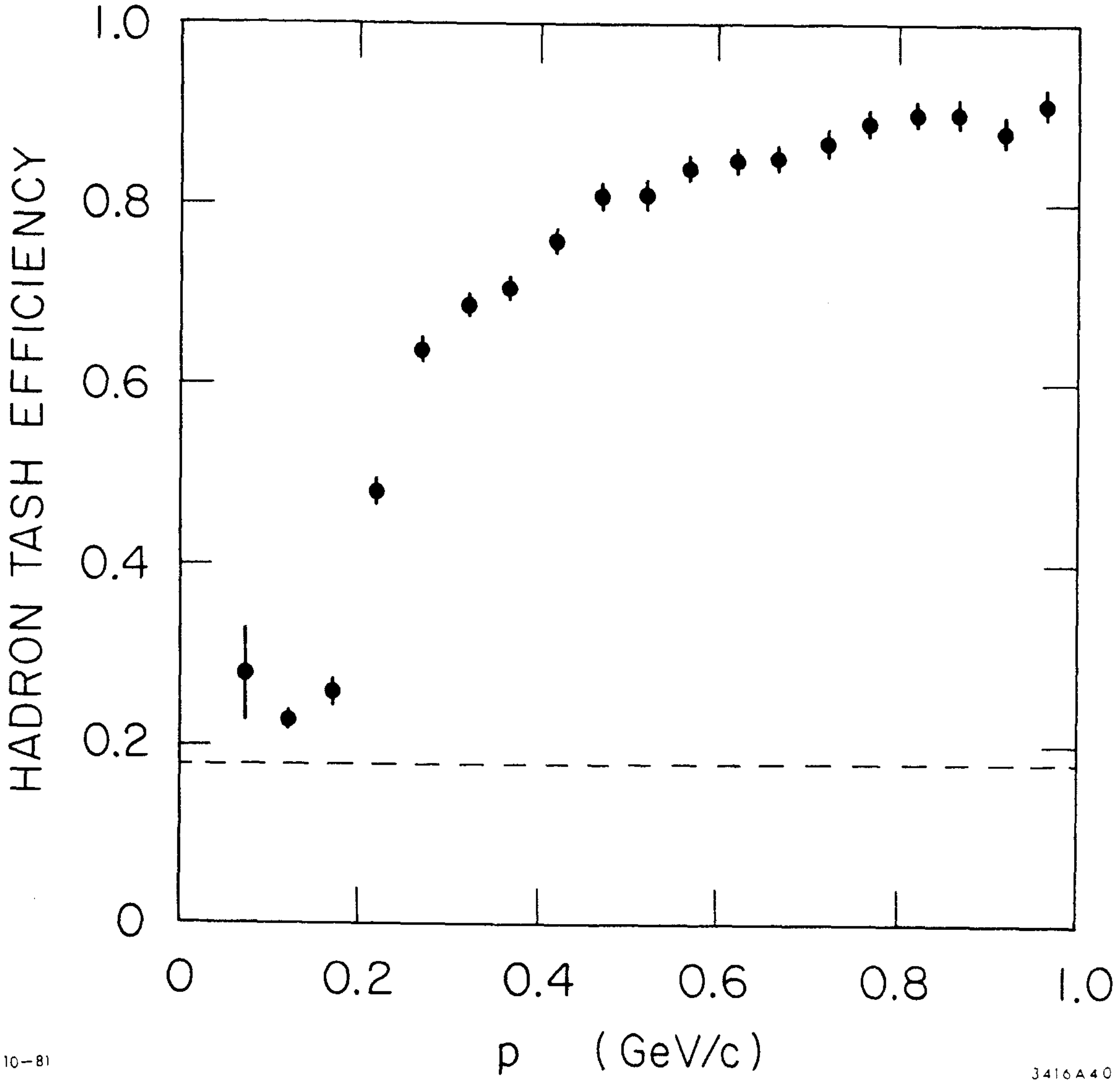
HADRON TASH EFFICIENCY
1.0
0.8
0.6
0.4
0.2
0
0
0.2
0.4
0.6
0.8
1.0
p (GeV/c)
10-81
3416A40

Fig. 4

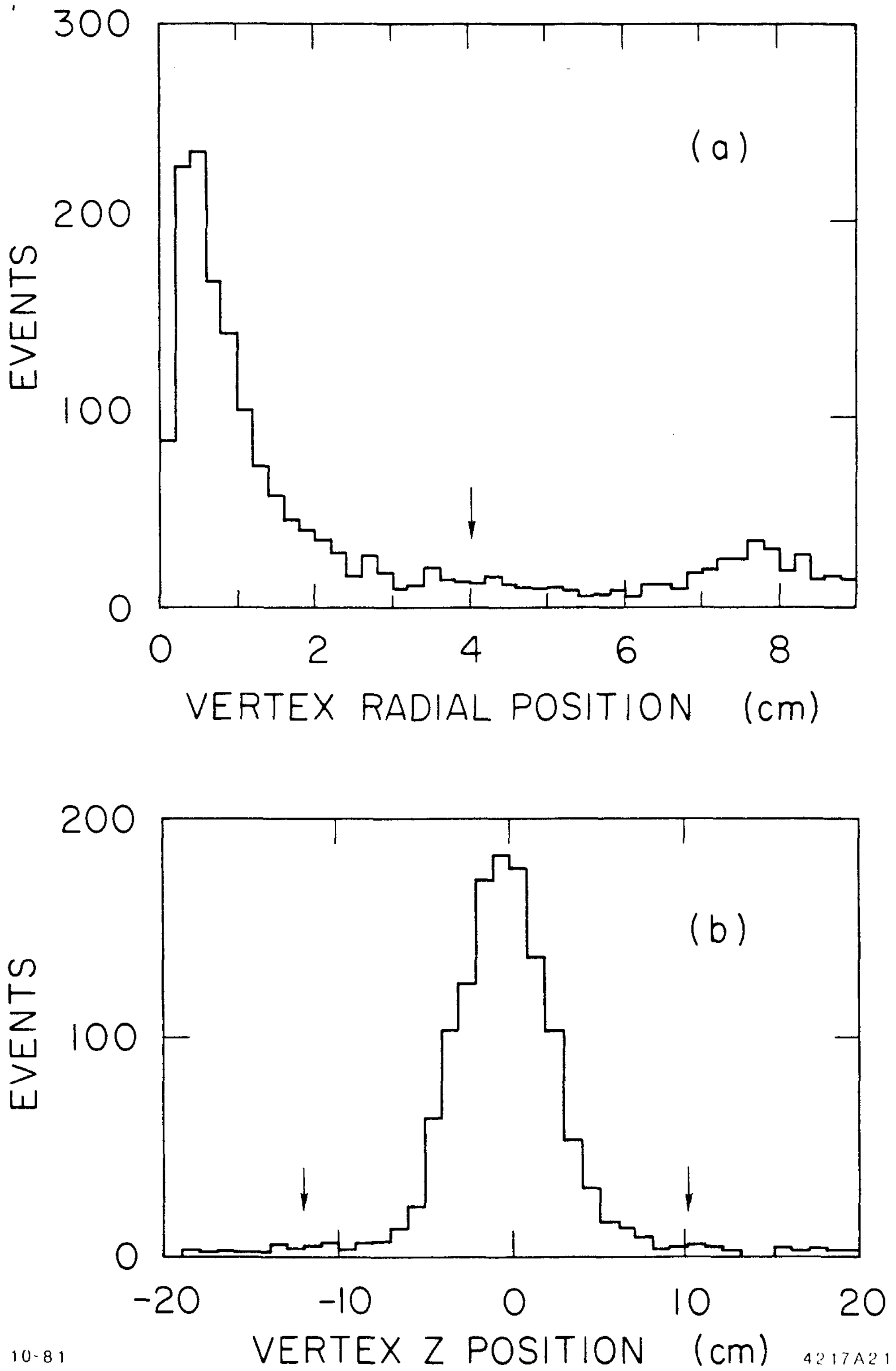
300
200
100
0
EVENTS
(a)
0
2
4
6
8
VERTEX RADIAL POSITION (cm)
200
100
0
EVENTS
(b)
-20
-10
0
10
20
VERTEX Z POSITION (cm)
10-81
4217A21

Fig. 5

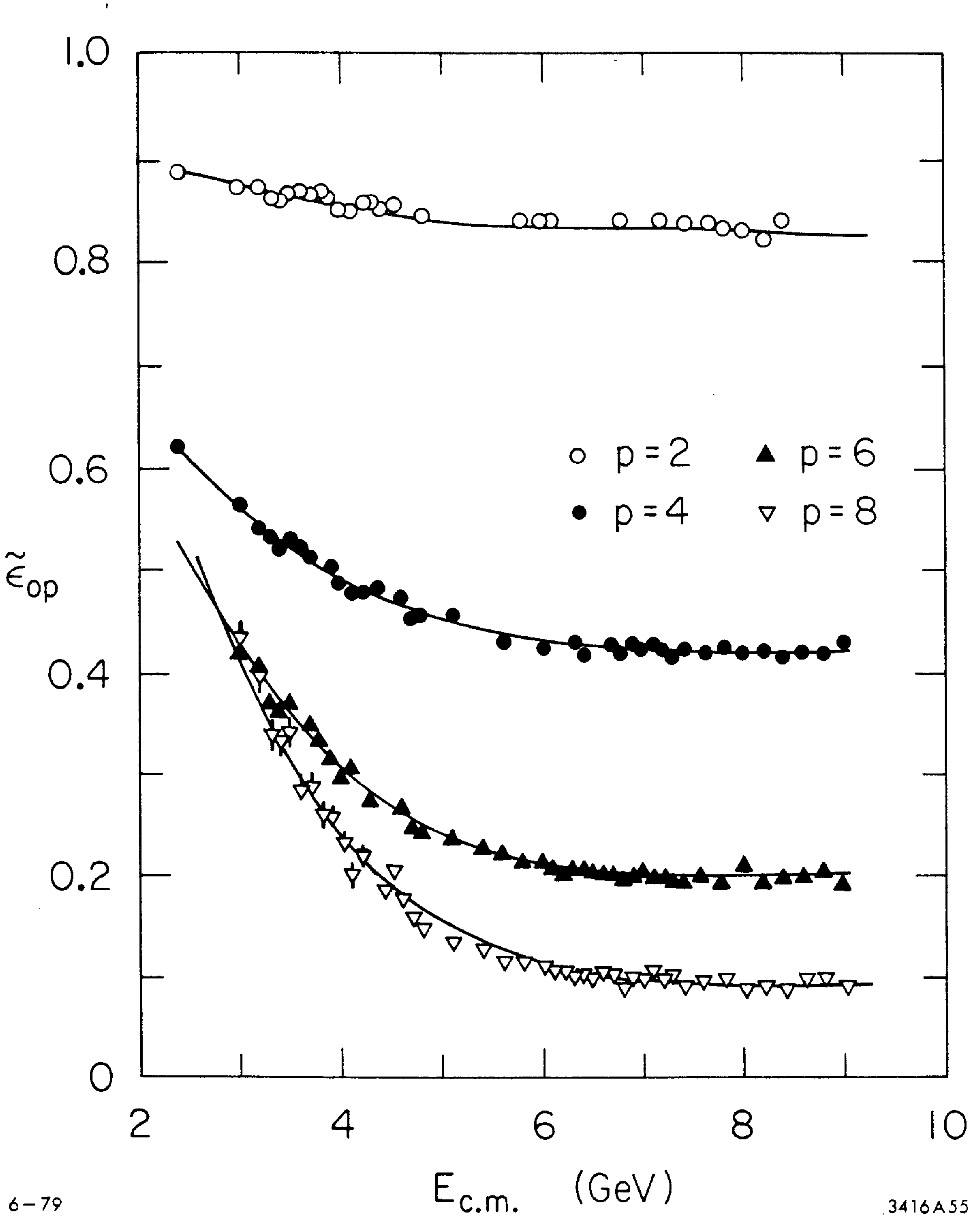

1.0
0.8
0.6
0.4
0.2
0
$\tilde{\epsilon}_{op}$
○ p=2
● p=4
▲ p=6
▽ p=8
2
4
6
8
10
$E_{c.m.}$ (GeV)
6–79
3416A55

Fig. 6

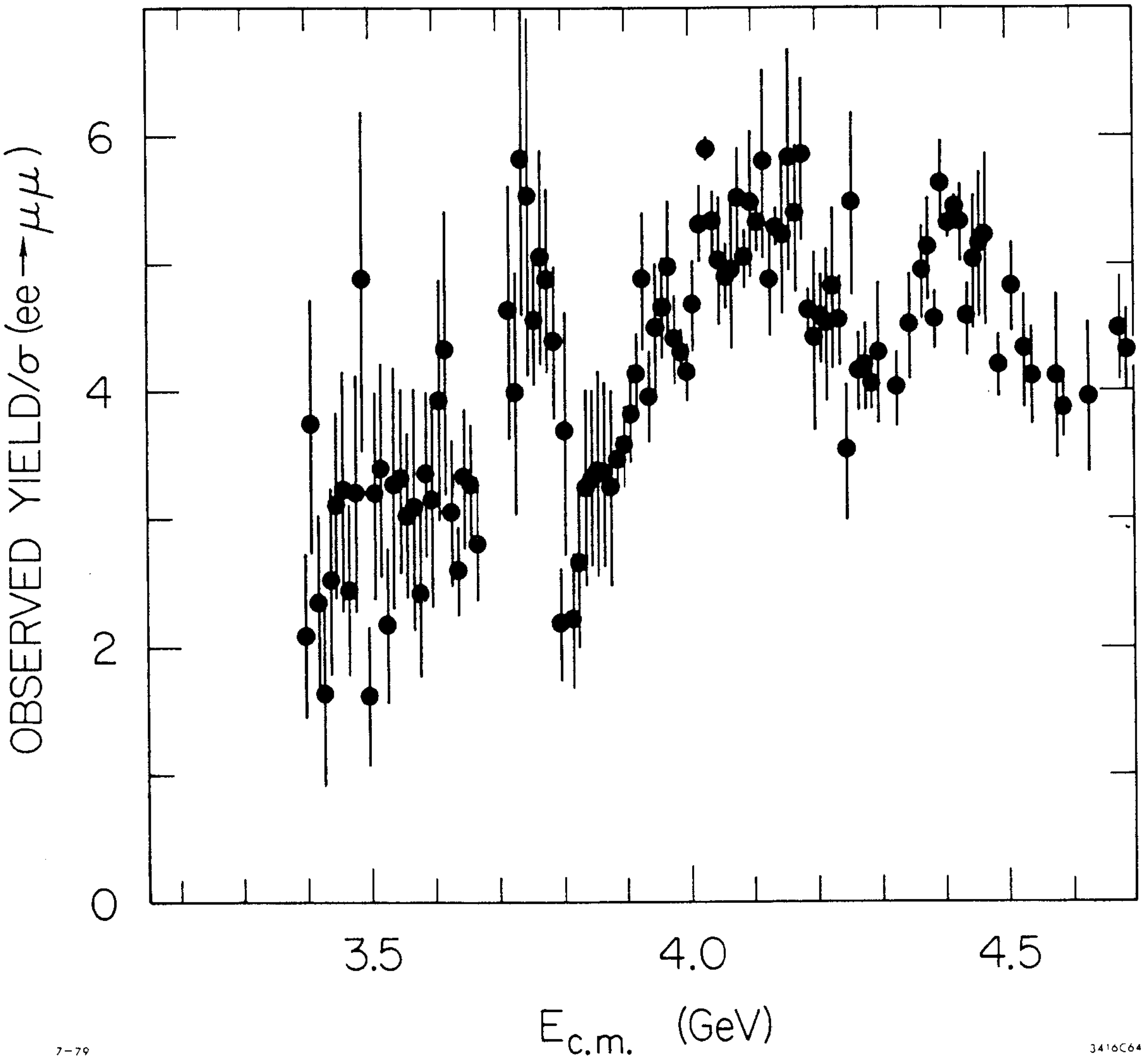

Fig. 7

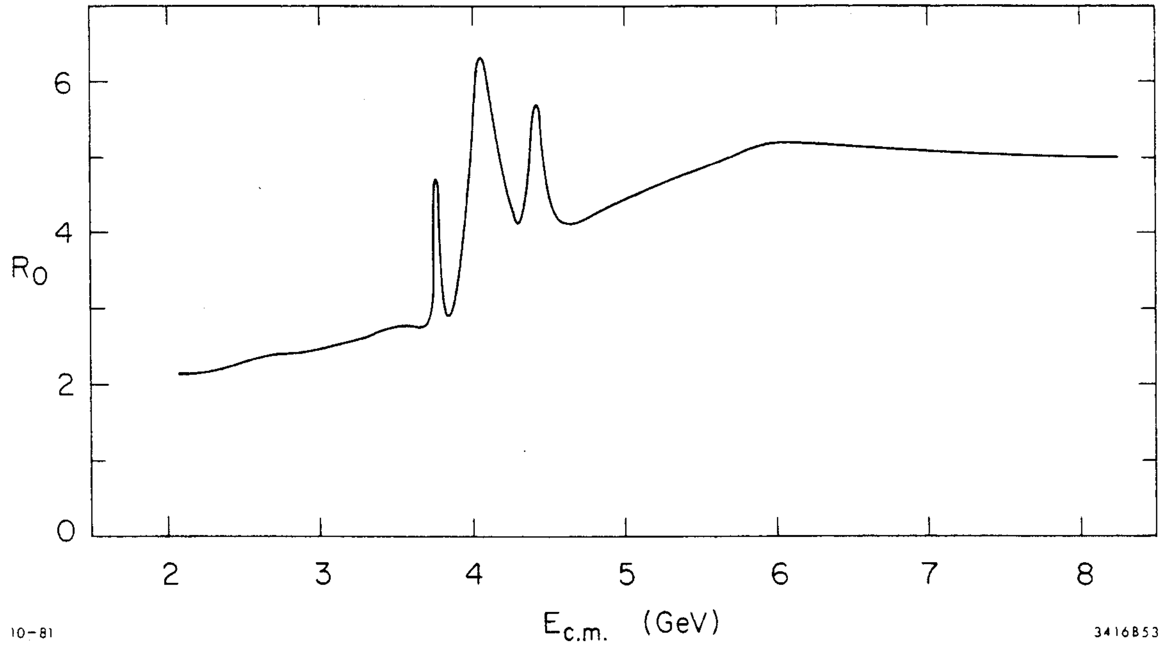

Fig. 8

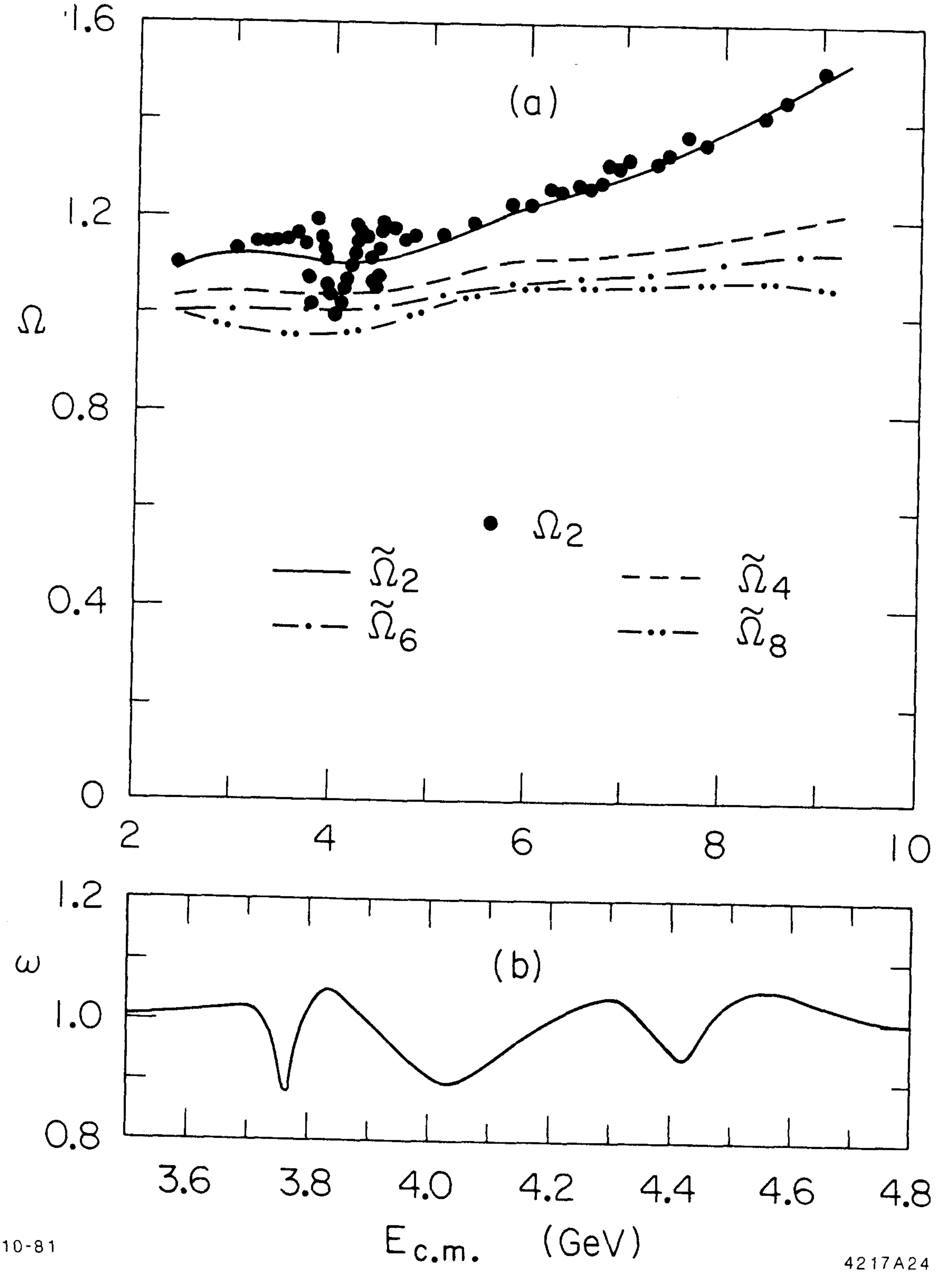
1.6
1.2
0.8
0.4
0
Ω
(a)
● Ω_2
$\tilde{\Omega}_2$
$\tilde{\Omega}_4$
$\tilde{\Omega}_6$
$\tilde{\Omega}_8$
2
4
6
8
10
1.2
1.0
0.8
ω
(b)
3.6
3.8
4.0
4.2
4.4
4.6
4.8
$E_{c.m.}$ (GeV)
10-81
4217A24

Fig. 9

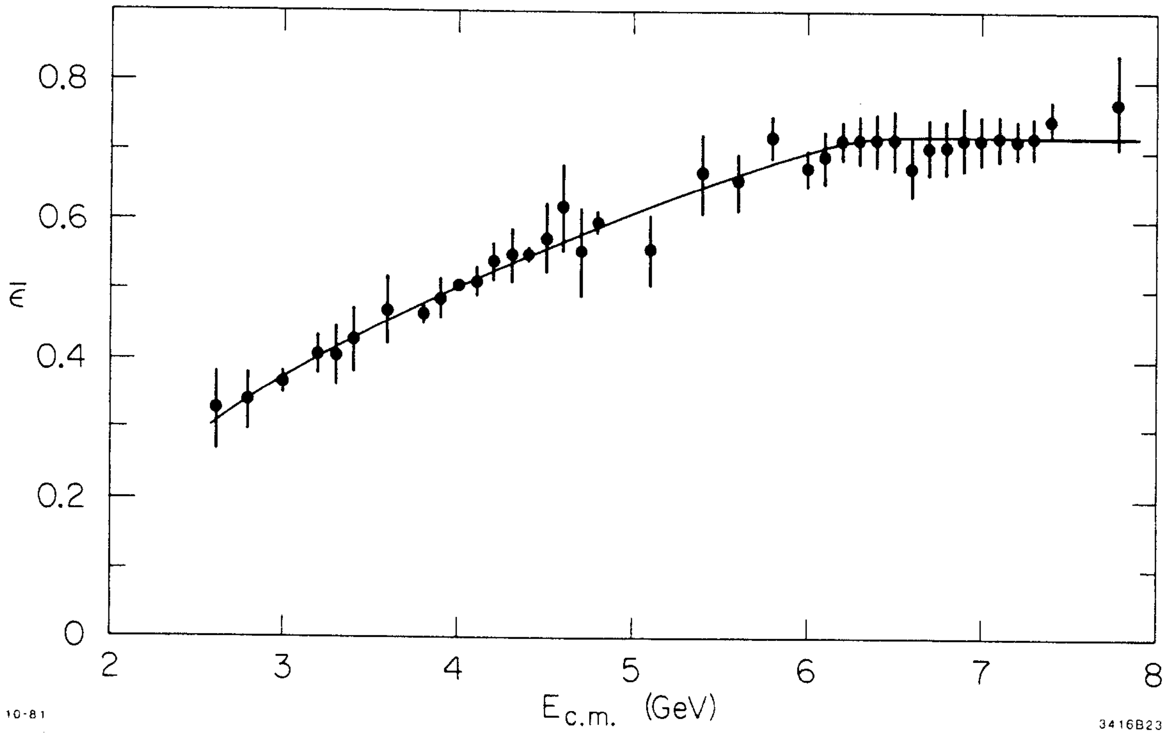

Fig. 10

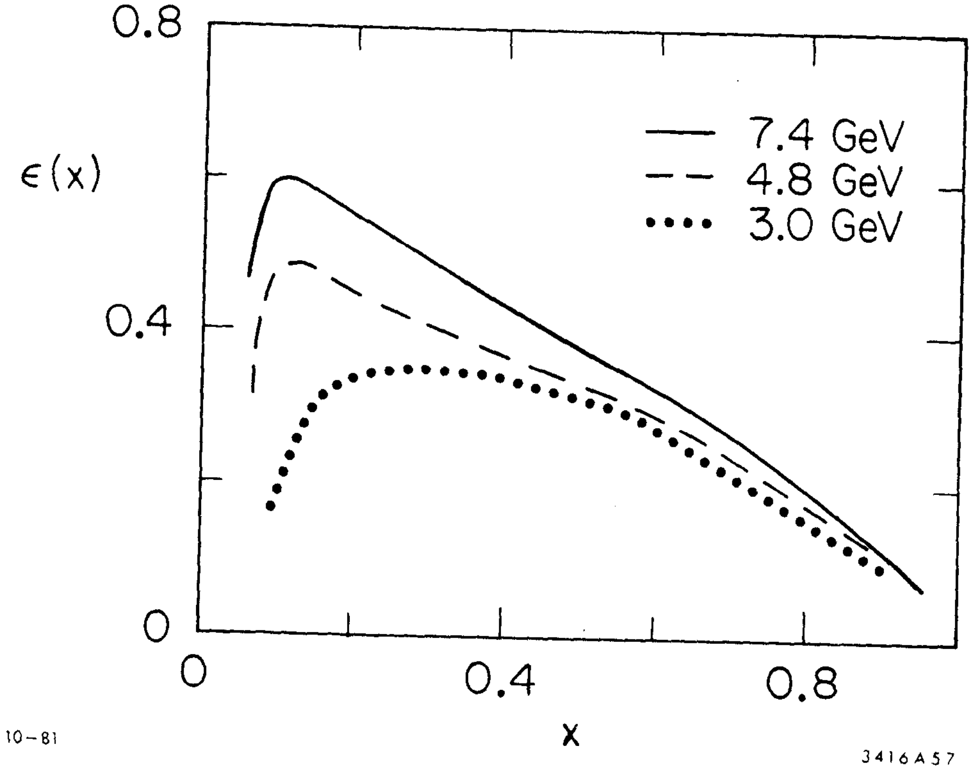

Fig. 11

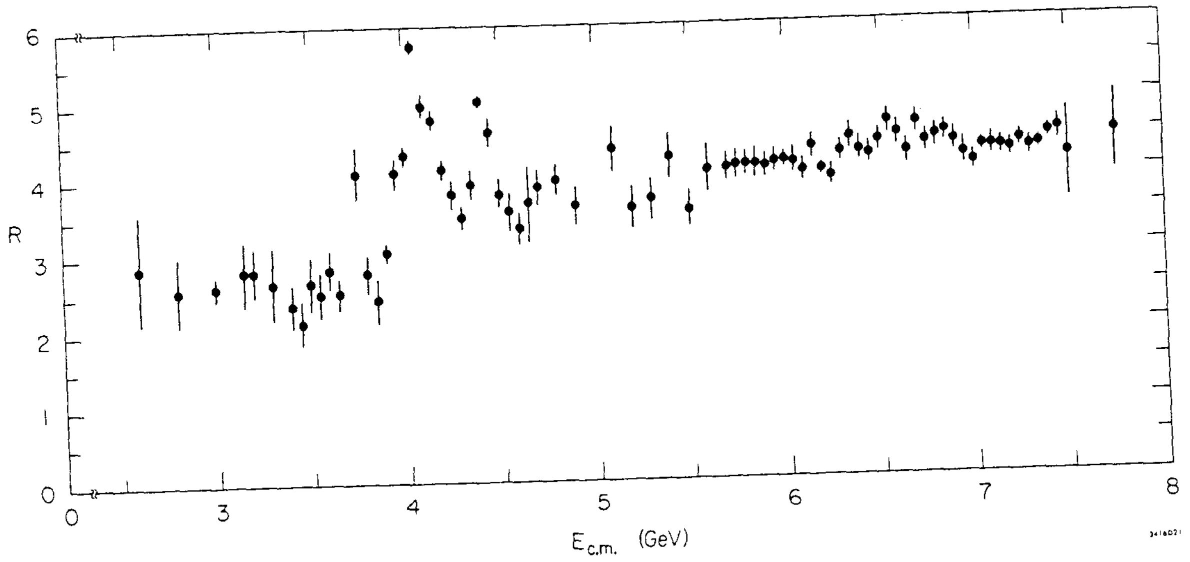

Fig. 12

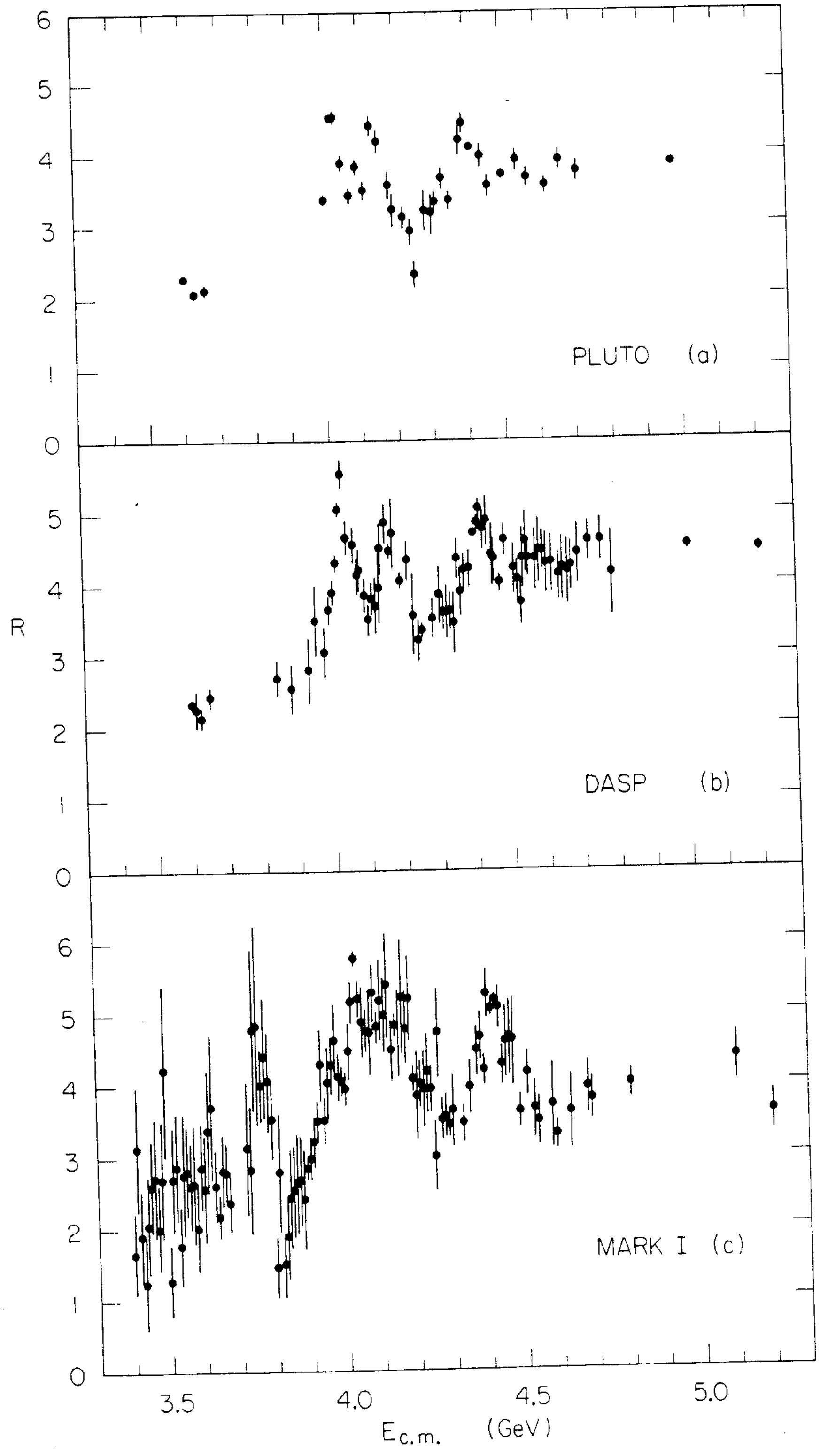
6
5
4
3
2
1
0
PLUTO (a)
5
4
R
3
2
1
0
DASP (b)
6
5
4
3
2
1
0
MARK I (c)
3.5
4.0
4.5
5.0
$E_{c.m.}$ (GeV)

Fig. 13

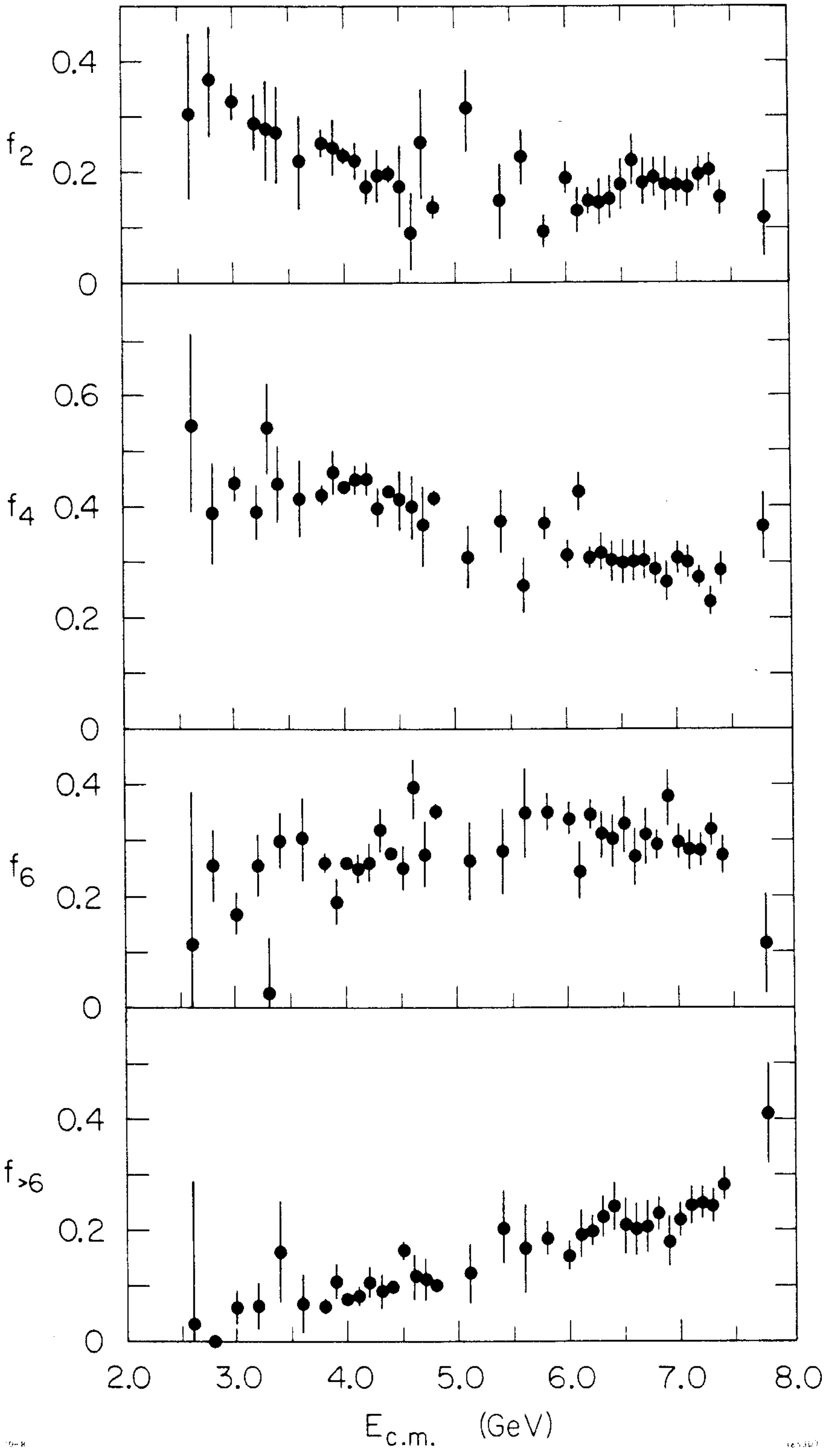

f2
0.4
0.2
0
f4
0.6
0.4
0.2
0
f6
0.4
0.2
0
f>6
0.4
0.2
0
2.0
3.0
4.0
5.0
6.0
7.0
8.0
Ec.m. (GeV)

Fig. 14

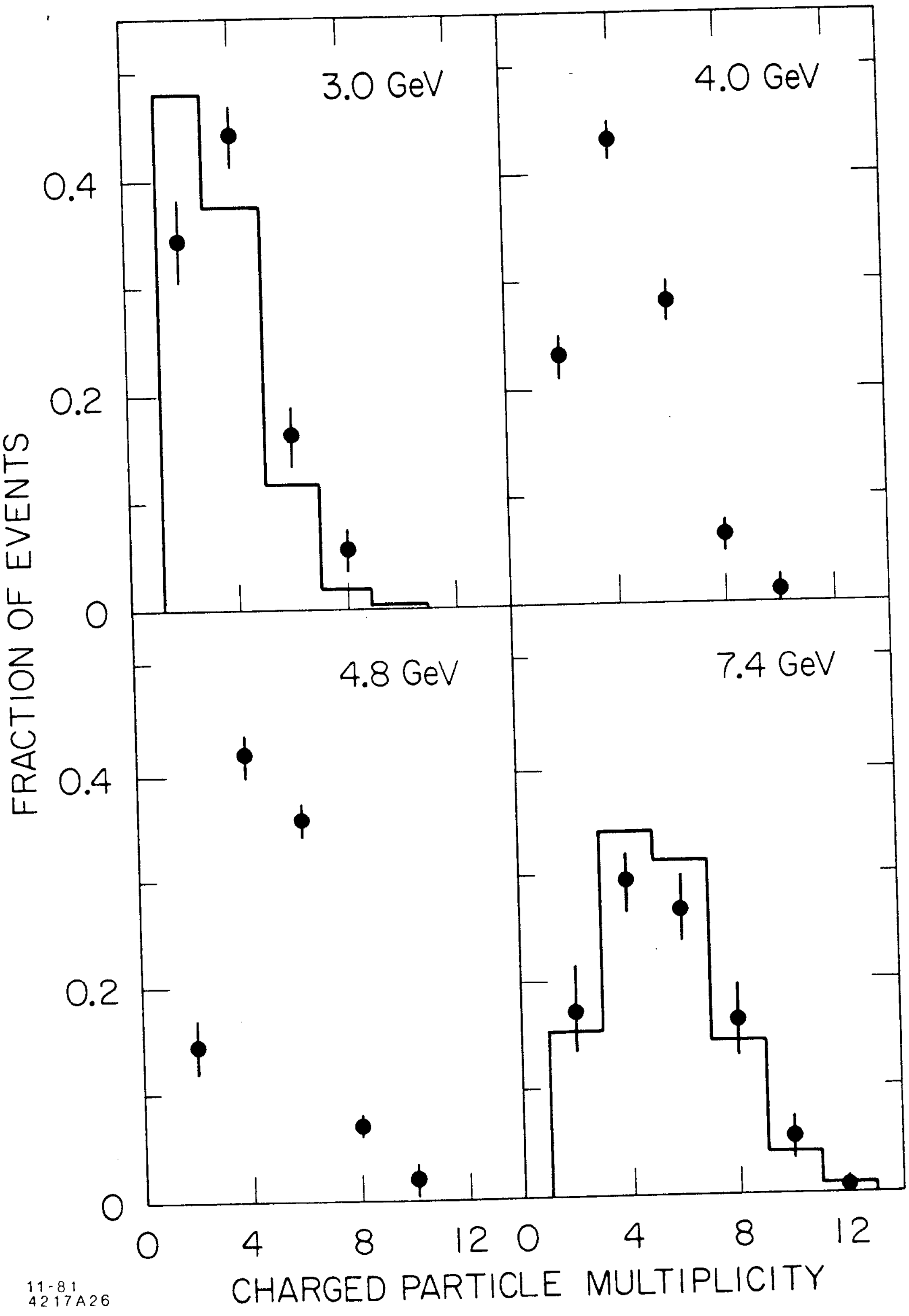
3.0 GeV
4.0 GeV
4.8 GeV
7.4 GeV
0.4
0.2
0
FRACTION OF EVENTS
0
4
8
12
CHARGED PARTICLE MULTIPLICITY
11-81
4217A26

Fig. 15

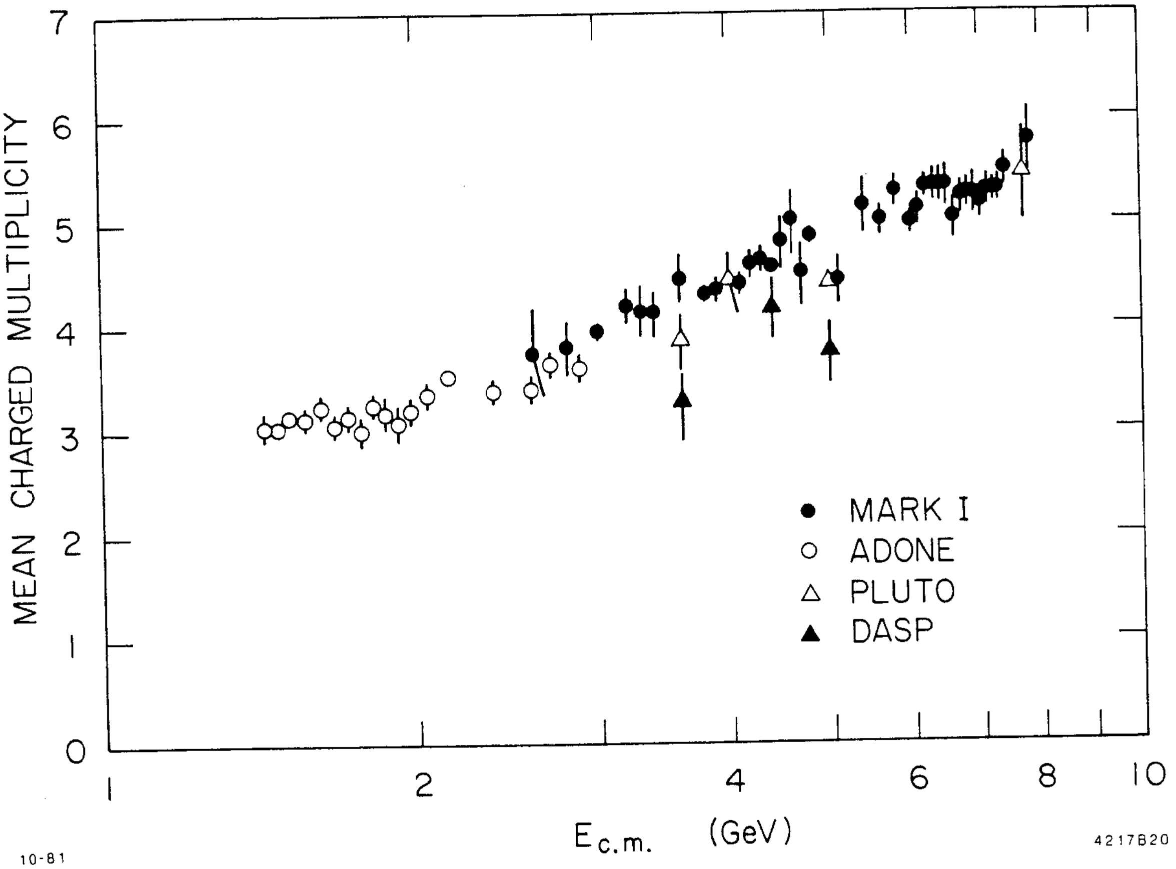

MEAN CHARGED MULTIPLICITY
0
1
2
3
4
5
6
7
1
2
4
6
8
10
E$_{c.m.}$ (GeV)
● MARK I
○ ADONE
△ PLUTO
▲ DASP
10-81
4217B20

Fig. 16

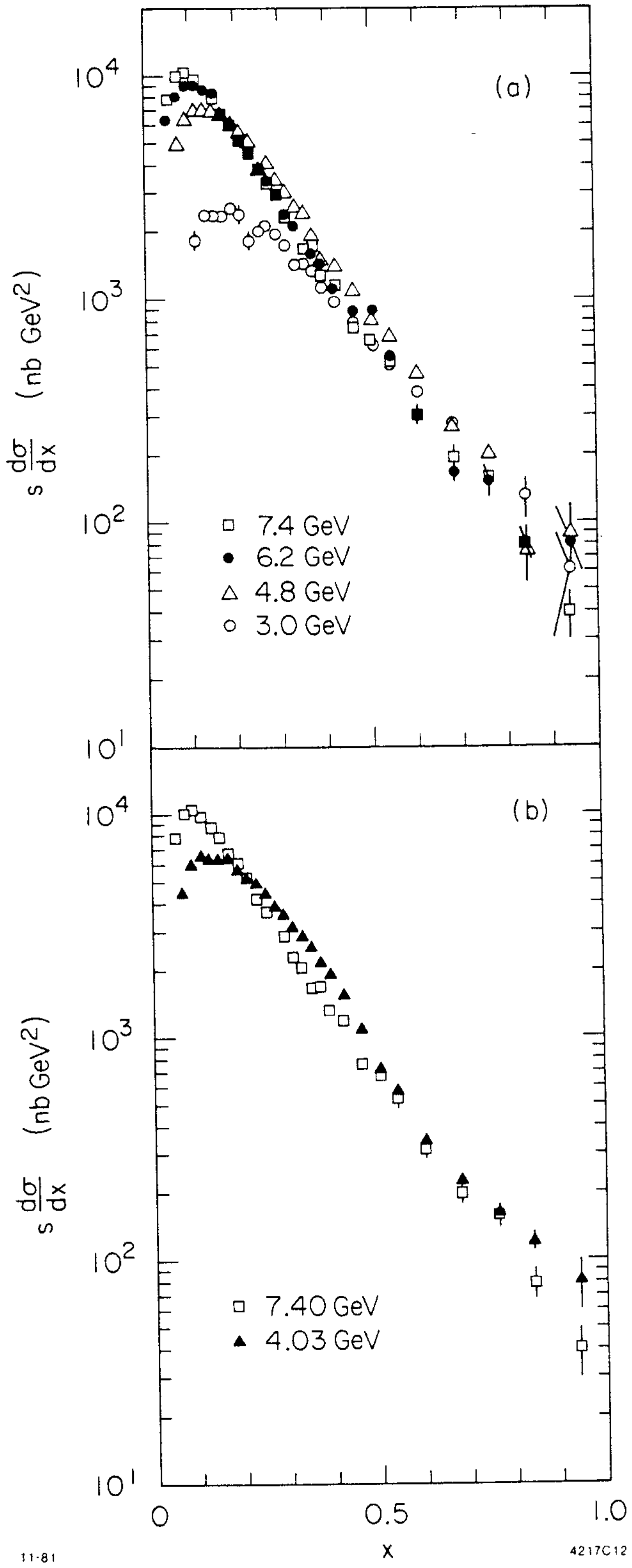

(a)
10^4
10^3
10^2
10^1
$s\frac{d\sigma}{dx}$ (nb GeV^2)
□ 7.4 GeV
● 6.2 GeV
△ 4.8 GeV
○ 3.0 GeV
(b)
□ 7.40 GeV
▲ 4.03 GeV
0
0.5
1.0
x
11-81
4217C12

Fig. 17

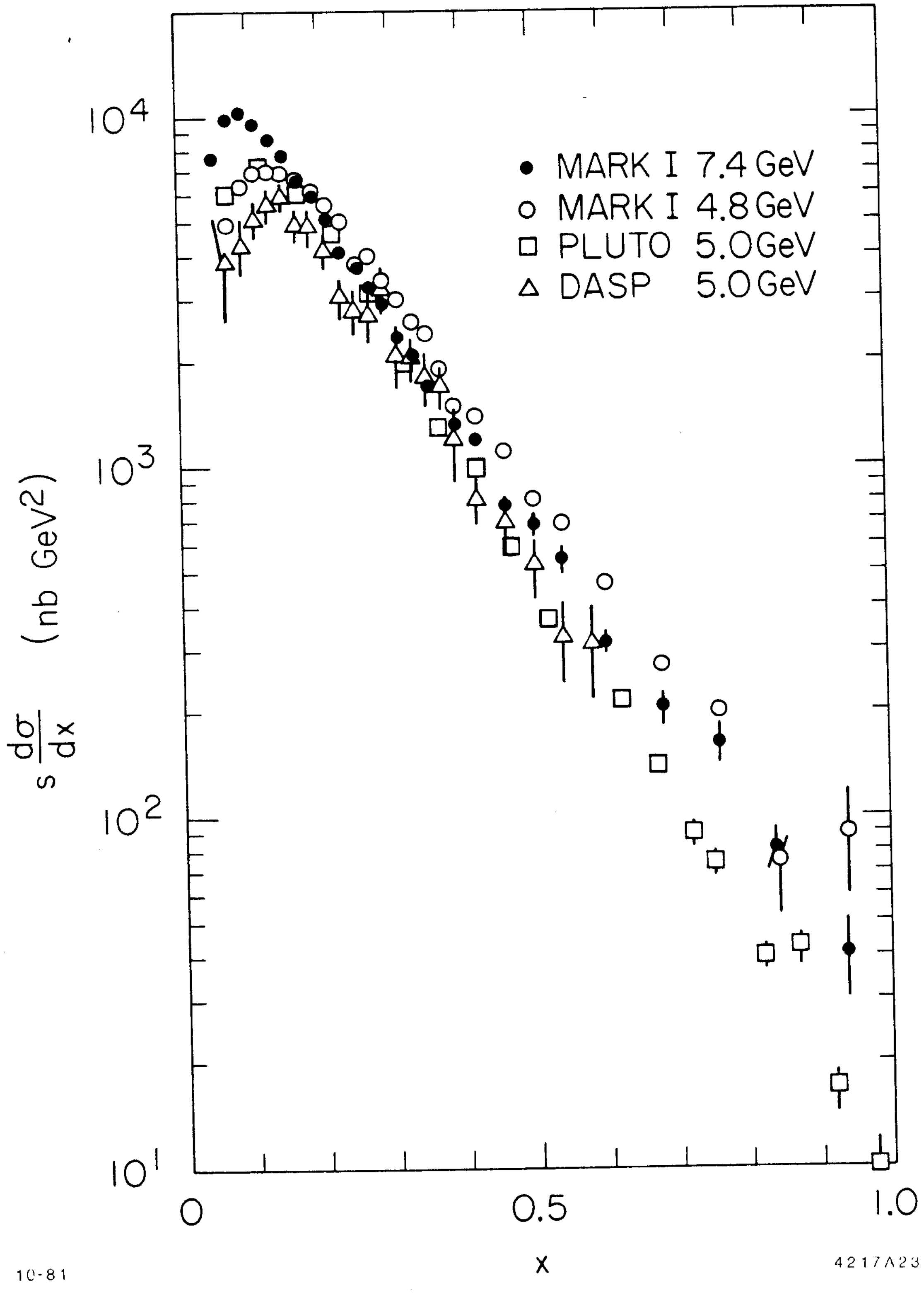

● MARK I 7.4 GeV
○ MARK I 4.8 GeV
□ PLUTO 5.0 GeV
△ DASP 5.0 GeV
$s\frac{d\sigma}{dx}$ (nb GeV^2)
10^4
10^3
10^2
10^1
0
0.5
1.0
x
10-81
4217A23

Fig. 18

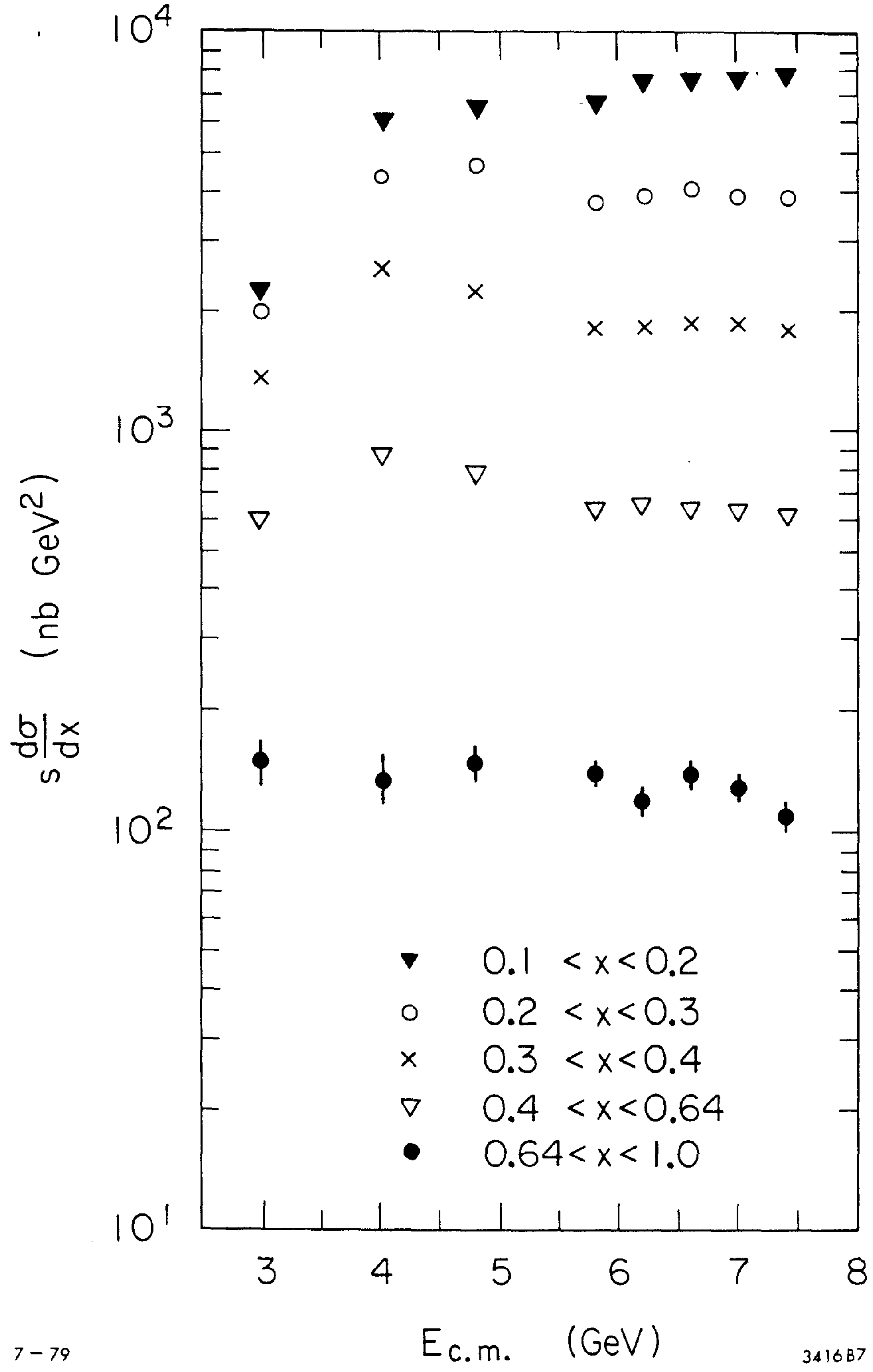

10^4
10^3
10^2
10^1
$s\frac{d\sigma}{dx}$ (nb GeV^2)
3
4
5
6
7
8
Ec.m. (GeV)
▼ 0.1 < x < 0.2
○ 0.2 < x < 0.3
× 0.3 < x < 0.4
▽ 0.4 < x < 0.64
● 0.64 < x < 1.0
7 – 79
3416B7

Fig 19

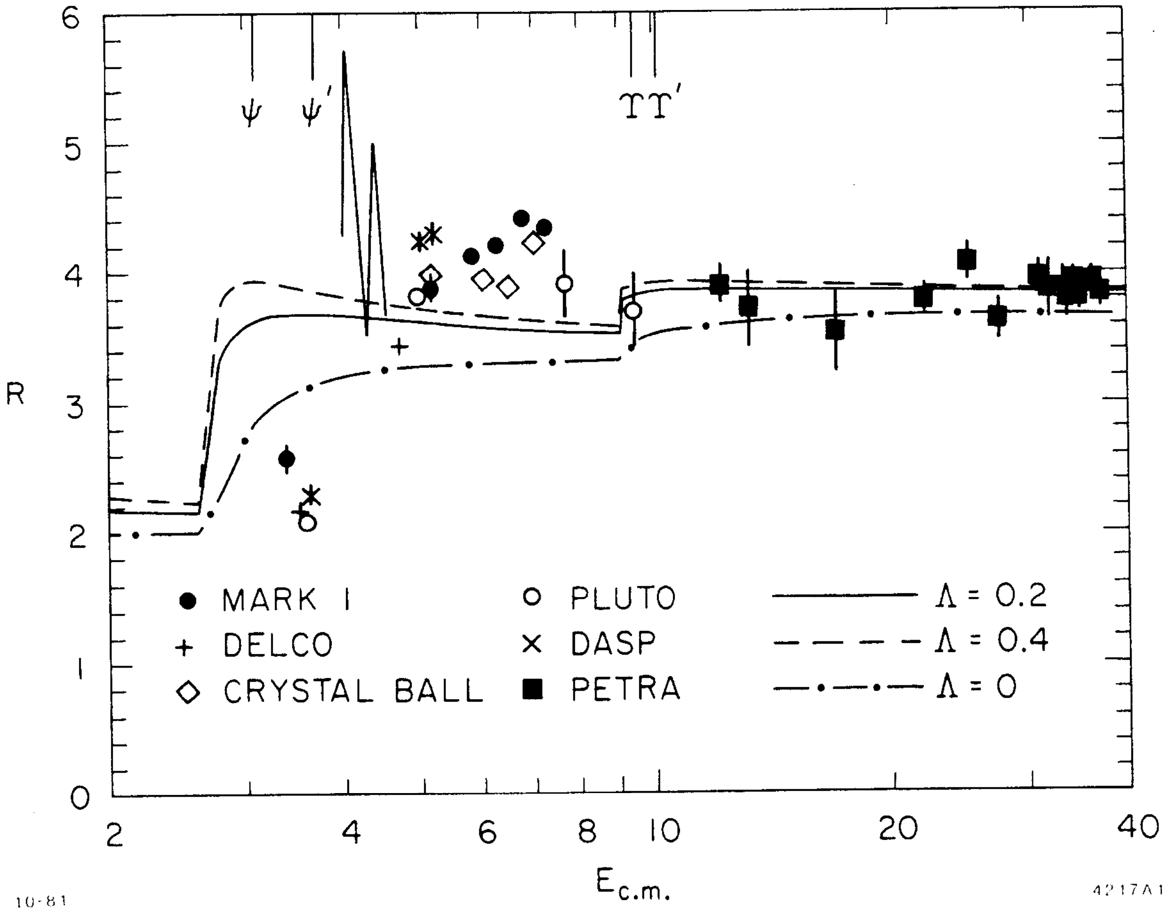

6
5
4
3
2
1
0
R
ψ
ψ′
ϒ ϒ′
● MARK I
+ DELCO
◇ CRYSTAL BALL
○ PLUTO
× DASP
■ PETRA
Λ = 0.2
Λ = 0.4
Λ = 0
2
4
6
8
10
20
40
$E_{c.m.}$
10-81
4217A1

Fig. 20